



Report SPR-P1(15) M017

Final Report
26-1121-4022-001

Evaluation of Thin Asphalt Overlay Practice Preserving Nebraska's Asphalt Pavements

Taesun You, Ph.D.

Postdoctoral Research Associate
Department of Civil Engineering
University of Nebraska-Lincoln

Soohyok Im, Ph.D.

Assistant Transportation Researcher
Texas A&M Transportation Institute

Yong-Rak Kim, Ph.D.

Associate Professor
University of Nebraska-Lincoln

Hamzeh Haghshenas

Gabriel Nsengiyumva

2015

Nebraska Transportation Center
262 WHIT
2200 Vine Street
Lincoln, NE 68583-0851
(402) 472-1975

"This report was funded in part through grant[s] from the Federal Highway Administration [and Federal Transit Administration], U.S. Department of Transportation. The views and opinions of the authors [or agency] expressed herein do not necessarily state or reflect those of the U.S. Department of Transportation."

Evaluation of Thin Asphalt Overlay Practice Preserving Nebraska's Asphalt Pavements

Taesun You, Ph.D.
Postdoctoral Research Associate
Department of Civil Engineering
University of Nebraska-Lincoln

Hamzeh Haghshenas
Graduate Research Assistant
Department of Civil Engineering
University of Nebraska-Lincoln

Soohyok Im, Ph.D.
Assistant Transportation Researcher
Texas A&M Transportation Institute

Gabriel Nsengiyumva
Graduate Research Assistant
Department of Civil Engineering
University of Nebraska-Lincoln

Yong-Rak Kim, Ph.D.
Associate Professor
Department of Civil Engineering
University of Nebraska-Lincoln

A Report on Research Sponsored by

Nebraska Department of Roads

June 2015

Technical Report Documentation Page

1. Report No. SPR-P1(15) M017		2. Government Accession No.		3. Recipient's Catalog No.	
4. Title and Subtitle Evaluation of Thin Asphalt Overlay Practice Preserving Nebraska's Asphalt Pavements			5. Report Date June 2015		
			6. Performing Organization Code		
7. Author(s) Taesun You, Soohyok Im, Yong-Rak Kim, Hamzeh Haghshenas, and Gabriel Nseniyumva			8. Performing Organization Report No. 26-1121-4022-001		
9. Performing Organization Name and Address University of Nebraska-Lincoln, Department of Civil Engineering 362M Whittier Research Center, Lincoln, NE 68583-0856			10. Work Unit No. (TRAIS)		
			11. Contract or Grant No.		
12. Sponsoring Agency Name and Address Nebraska Department of Roads 1500 Highway 2, PO Box 94759, Lincoln, NE 68509			13. Type of Report and Period Covered		
			14. Sponsoring Agency Code		
15. Supplementary Notes					
<p>16. Abstract</p> <p>This study examined the current thin asphalt overlay practices implemented in Nebraska. To that end, the mechanical properties and performance characteristics of the two mixtures (i.e., SLX and SPH) were compared by carrying out laboratory tests such as dynamic modulus test, dynamic creep test, static creep-recovery test, semi-circular bending test, and Hamburg wheel tracking test. The laboratory test results were also used to characterize the material properties for pavement performance prediction simulation. Structural performance analysis was conducted using the MEPDG and finite element method in order to compare the pavement structures with the two different mixtures (i.e., SLX and SPH). In addition, a life-cycle cost analysis (LCCA) was performed to compare the economic benefits associated with the thin-lift overlay to the conventional overlay practice. This provided insights into how the thin asphalt overlay with the SLX mixture behaved compared to the previous practice, which replaced the old asphalt with the SPH mixture. Laboratory results clearly showed that the SLX mixture behaved similarly to the SPH mixture in terms of mixture stiffness, rutting potential, and cracking resistance. However, the Hamburg wheel tracking test found that the SLX mixture had greater moisture susceptibility, a result that requires more investigation. Pavement performance simulation results from finite element analysis showed that the rutting and cracking potential of the pavement with SLX thin overlay mixture was lower than the pavement with SPH mixture. MEPDG simulations predicted that both pavements would perform satisfactorily during their expected design life, but the LCCA indicated that the practice of using the thin SLX preservation technique can reduce both the agency's and user's costs compared to the conventional SPH rehabilitation practice. Both performance prediction results need to be compared to actual field performance data. Only one-year field performance is available to date, which needs to be continuously monitored to judge how both pavement structures perform.</p>					
17. Key Words Add key words here			18. Distribution Statement		
19. Security Classif. (of this report) Unclassified		20. Security Classif. (of this page) Unclassified		21. No. of Pages 78	22. Price

Form DOT F 1700.7 (8-72) Reproduction of form and completed page is authorized

Table of Contents

Acknowledgements.....	vi
Disclaimer.....	vii
Abstract.....	viii
Chapter 1 Introduction.....	1
1.1 Research Objectives and Scope	3
1.2 Organization of the Report.....	3
Chapter 2 Background.....	4
2.1 Benefits of Thin Asphalt Overlays	4
2.2 Specifications of Thin Asphalt Overlay Materials, Mixtures, and Structures	6
2.2.1 Aggregate.....	6
2.2.2 Binder.....	8
2.2.3 Volumetric mix design.....	8
2.2.4 Thin asphalt overlay thickness and its service life.....	9
2.3 Laboratory Performance Tests.....	10
2.4 Pavement Performance Predictions	12
Chapter 3 Material Selection and Sample Fabrication	16
3.1 Materials	16
3.2 Specimen Fabrication.....	19
3.2.1 Dynamic modulus, dynamic creep, and static creep-recovery test specimens ..	19
3.2.2 Semi-circular bend fracture test specimens	20
3.2.3 Hamburg wheel tracking test specimens.....	20
Chapter 4 Laboratory Tests and Data Analysis	22
4.1 Dynamic Modulus Test and Results	22
4.2 Dynamic Creep Test and Results	24
4.3 Static Creep-Recovery Test and Results.....	26
4.4 SCB Fracture Test and Results	28
4.5 Hamburg Wheel Tracking Test and Results	31
Chapter 5 Characterization of Material Properties	34
5.1 Viscoelastic Material Properties	34
5.2 Viscoplastic Material Properties	35
5.3 Fracture Properties	37
5.4 Viscodamage Material Properties	38
Chapter 6 Pavement Performance Predictions	39
6.1 MEPDG Simulation.....	42
6.2 Life Cycle Cost Analysis (LCCA) and Results	43
6.3 Finite Element Modeling	47
6.3.1 Pavement model geometry and boundary conditions	47
6.3.2 Layer properties	51
6.3.3 Simulation results.....	53
Chapter 7 Summary and Conclusions	60
References.....	62
Appendix A.....	67
A.1 Viscoelastic Material Properties	67
A.2 Viscoplastic Material Properties	69
A.3 Fracture Properties	72

A.4 Viscodamage Material Properties 75

List of Figures

Figure 2.1 Typical unit costs and pavement life for specific maintenance and preservation treatments (Brown and Heitzman 2013).....	6
Figure 2.2 Reflective crack modeling in HMA overlay (Baek and Al-Qadi 2009).....	14
Figure 2.3 Finite element model (Dave and Buttlar 2010).....	15
Figure 2.4 Finite element model (Ahmed et al. 2013).....	15
Figure 3.1 Aggregate gradation of the mixtures.....	18
Figure 3.2 Picture of mixture microstructures.....	18
Figure 3.3 Specimen fabrication and uniaxial testing configuration.....	19
Figure 3.4 SCB specimen fabrication and fracture testing configuration.....	20
Figure 3.5 Hamburg wheel tracking test specimen sawn and mounting system.....	21
Figure 4.1 Dynamic modulus test results.....	24
Figure 4.2 Dynamic creep test results.....	25
Figure 4.3. Repeated creep-recovery test results of each mixture.....	28
Figure 4.4 SCB test results.....	31
Figure 4.5 Images of Hamburg wheel tracking test specimens after testing.....	32
Figure 4.6 Plot of Hamburg wheel tracking test results of each mixture.....	33
Figure 5.1 Hardening response of SPH and SLX.....	36
Figure 6.1 Project location: I-80 Exit 279 near Kearney, Nebraska.....	39
Figure 6.2 Pavement construction.....	40
Figure 6.3 Layer configuration of two pavement structures.....	41
Figure 6.4 Geometry and boundary condition for two pavement structures....	49
Figure 6.5 (a) Dual tire foot print (Yoo et al. 2006) and (b) three vertical pressures applied on the pavement structures.....	49
Figure 6.6 (a) Class 9 truck configuration (Soares et al. 2008) and (b) loading configuration for a vehicle speed of 60 mile/h.....	51
Figure 6.7 Node where rutting was measured in the pavement model.....	54
Figure 6.8 Comparison of rutting between SLX and SPH pavement structures with different old asphalt layer properties.....	55
Figure 6.9 Vertical displacement distribution contours of SLX and SPH pavement structures when 50% of SP5 viscoelastic property was used for old asphalt layer.....	56
Figure 6.10 Vertical displacement distribution contours of SLX and SPH pavement structures when 100% of SP5 viscoelastic property was used for old asphalt layer.....	57
Figure 6.11 Vertical displacement distribution contours of SLX and SPH pavement structures when 150% of SP5 viscoelastic property was used for old asphalt layer.....	58
Figure 6.12 Damage density distribution contours of SLX and SPH pavement structures when 150% of SP5 viscoelastic property was used for old asphalt layer.....	59
Figure A.1 Schematic illustration of FPZ of typical quasi-brittle materials.....	72
Figure A.2 A finite element modeling of the SCB testing.....	75
Figure A.3 Diagram of damage density rate and \bar{Y}/Y_0 at different strain levels and (b) diagram of damage density rate and the effective strain at different \bar{Y}/Y_0 values.....	78

List of Tables

Table 2.1 Decision matrix (Jahren et al. 2007).....	5
Table 2.2 NMAS requirements for a variety of states	7
Table 2.3 Aggregate quality requirements for a variety of states	7
Table 2.4 Comparative listing of bitumen in different states.....	8
Table 2.5 Mix design requirements in different states.....	9
Table 2.6 Comparative thickness and service life in different states and countries	10
Table 2.7 Summary of the laboratory tests	12
Table 2.8 Summary of the studies using MEPDG for the performance prediction of overlays ...	13
Table 3.1 SPH mixture information.....	17
Table 3.2 SLX mixture information.....	17
Table 4.1 Summary of Hamburg wheel tracking test results of each mixture.....	33
Table 5.1 Obtained viscoelastic properties.....	35
Table 5.2 Identified viscoplastic material properties ($T_{ref}=21^{\circ}\text{C}$).....	36
Table 5.3 Cohesive zone fracture properties.....	37
Table 5.4 Viscodamage material properties ($T_{ref}= 21^{\circ}\text{C}$).....	38
Table 6.1 Summary of key inputs of MEPDG simulations and results.....	43
Table 6.2 Summary of cost inputs for each alternative and detail traffic inputs.....	45
Table 6.3 Summary of the LCCA analysis results.....	47
Table 6.4 Dual tire configuration for each rib (Yoo et al. 2006).....	49
Table 6.5 Material properties of each layer.....	52

Acknowledgements

The authors thank the Nebraska Department of Roads (NDOR) for the financial support needed to complete this study. In particular, the authors thank NDOR Technical Advisory Committee (TAC) for their technical support and invaluable discussions/comments.

Disclaimer

This report was funded in part through grant[s] from the Federal Highway Administration [and Federal Transit Administration], U.S. Department of Transportation. The views and opinions of the authors [or agency] expressed herein do not necessarily state or reflect those of the U. S. Department of Transportation.

Abstract

This study examined the current thin asphalt overlay practices implemented in Nebraska. To that end, the mechanical properties and performance characteristics of the two mixtures (i.e., SLX and SPH) were compared by carrying out laboratory tests such as dynamic modulus test, dynamic creep test, static creep-recovery test, semi-circular bending test, and Hamburg wheel tracking test. The laboratory test results were also used to characterize the material properties for pavement performance prediction simulation. Structural performance analysis was conducted using the MEPDG and finite element method in order to compare the pavement structures with the two different mixtures (i.e., SLX and SPH). In addition, a life-cycle cost analysis (LCCA) was performed to compare the economic benefits associated with the thin-lift overlay to the conventional overlay practice. This provided insights into how the thin asphalt overlay with the SLX mixture behaved compared to the previous practice, which replaced the old asphalt with the SPH mixture. Laboratory results clearly showed that the SLX mixture behaved similarly to the SPH mixture in terms of mixture stiffness, rutting potential, and cracking resistance. However, the Hamburg wheel tracking test found that the SLX mixture had greater moisture susceptibility, a result that requires more investigation. Pavement performance simulation results from finite element analysis showed that the rutting and cracking potential of the pavement with SLX thin overlay mixture was lower than the pavement with SPH mixture. MEPDG simulations predicted that both pavements would perform satisfactorily during their expected design life, but the LCCA indicated that the practice of using the thin SLX preservation technique can reduce both the agency's and user's costs compared to the conventional SPH rehabilitation practice. Both performance prediction results need to be compared to actual field performance data. Only one-

year field performance is available to date, which needs to be continuously monitored to judge how both pavement structures perform.

Chapter 1 Introduction

Pavement preservation is a cost-effective technique that extends pavement life, improves safety, and meets motorist expectations (FHWA 2006). There are several techniques for preserving asphalt pavements, including chip seals, slurry seals, microsurfacing, fog seals, crack treatment, and thin asphalt overlays. Among the techniques mentioned above, thin asphalt overlays are typically 38.1 mm or less (1.5 inch or less) in thickness, and they are comprised of finer aggregates (a nominal maximum aggregate size [NMAS] of 12.5 mm or less) compared to the aggregates in typical Superpave asphalt mixtures (Newcomb 2009).

Also known as “thin lifts,” thin asphalt overlays offer an economical resurfacing, preservation, and renewal paving solution for roads requiring safety and smoothness improvements. Thin asphalt overlays not only provide a new pavement surface for a fraction of the cost of rebuilding a roadway, but they are also the only preventive maintenance technique that simultaneously improves the structural value and extends the pavement's service life. Although thin asphalt overlays are more expensive in initial cost compared to other proven pavement preservation surface treatments (e.g., microsurfacing or chip seals) (Brown and Heitzman 2013), proponents affirm that they provide an increased smoothness with a quieter ride than the other surface treatments in the short term. Additionally, their durability is higher in the long term, which is due to a slight structural enhancement to the pavement (Newcomb 2009).

Thin asphalt overlay applications are most effective for roads in good structural condition that need resurfacing due to cracking, raveling, rutting, aging, oxidation, or minor disintegration. It is noteworthy that thin asphalt overlays are not considered a solution for roadways requiring significant structural rehabilitation, but are common techniques for pavement preservation. Thin

asphalt overlays improve ride quality, decrease pavement distresses, maintain surface geometrics, mitigate noise levels, reduce life cycle costs, and provide long-lasting service.

Among different types of thin lift overlays, thin hot-mix asphalt (HMA) overlay has gained popularity in recent years due to its long expected extended life and inexpensive annualized cost. Although the initial cost of thin HMA overlay is higher than some types of preserving layers (i.e. fog seals and crack seals), a low annualized cost of thin HMA overlay could be achieved due to long life extension (Brown and Heitzman 2013). Many states such as Texas (Scullion et al. 2009; Walubita and Scullion 2008; Wilson et al. 2013), Michigan (MDOT 2005), Ohio (ODOT 2002), and New York (NYDOT 2008) attempted to use thinner HMA overlay to reduce the thickness of HMA overlay to less than 25.4 mm (1 inch).

Recently, thin asphalt overlays have been also implemented in the state of Nebraska as a promising pavement preservation technique. One inch thick asphalt concrete mix (SLX) is typically overlaid on top of the milled old asphalt layer. This new practice is different from the previous standard maintenance practice that usually removes the top two-inch of the old asphalt layer and replace the two-inch layer with a new asphalt mix (such as SPH or SPR). The SLX is usually designed with PG binder 64-34 by adding warm-mix asphalt (WMA) additive and 25-35% reclaimed asphalt pavement (RAP) materials. WMA adds further benefits to the mix by allowing the asphalt mix to be transported farther or constructed in cooler weather. RAP reduces the price of the mix and potentially enhances performance, especially rut resistance. The milling of the existing pavement surface can also enhance the overlay performance and provide recycled materials for the future.

Clearly, the new implementation of thin asphalt overlays is a promising pavement preservation strategy for our state in the future. The incorporation of WMA technology and RAP

in the mix is also highly desirable in terms of cost saving and the preservation of the environment and natural resources. Nonetheless, there is still a need to evaluate the current thin overlay practices to maximize their benefits and to judge if the new practice is adequate and/or comparable to the old rehabilitation practice in order to meet functional-structural performance expectations.

1.1 Research Objectives and Scope

The primary objective of this research is to evaluate the current thin asphalt overlay practices implemented in Nebraska. To that end, two mixtures (i.e., SLX and SPH) are compared by conducting laboratory tests that measure their mechanical properties and performance characteristics. The laboratory test results are also used in the MEPDG analysis and finite element modeling for predicting pavement performance behavior. This provides insight into how the one-inch thick asphalt overlay with SLX behaves compared to the previous practice, which replaced the old two-inch thick asphalt with a new mixture of SPH.

1.2 Organization of the Report

This report consists of seven chapters. Following the introduction chapter, chapter 2 summarizes the literature review on thin asphalt overlays. Chapter 3 describes material selection and sample fabrication processes. Chapter 4 introduces the laboratory tests conducted for the characterization of mechanical properties of SLX and SPH mixtures. These tests include the dynamic modulus, static multiple stress creep-recovery, dynamic creep, semicircular bending fracture, and Hamburg wheel tracking tests. In chapter 5, the material properties to conduct pavement performance simulations are identified. Chapter 6 describes the MEPDG predictions, LCCA, and finite element simulations of pavement performance. Finally, chapter 7 summarizes the main findings and major conclusions of this study.

Chapter 2 Background

Thin asphalt overlay is generally defined as a rehabilitation and preservation treatment layer with a thickness less than 38.1 mm (1.5 inches). The nominal maximum aggregate size (NMAS) in this type of preservation layers was less than 12.5 mm (0.5 inch) (Newcomb 2009). While this application can provide some structural strengthening, it is generally not used as a structural layer or designed to behave in a structural manner.

2.1 Benefits of Thin Asphalt Overlays

The National Asphalt Pavement Association (NAPA) reported several benefits of thin asphalt overlay applications (Newcomb 2009), including:

- long service life,
- low life cycle cost,
- minimized traffic delay due to less curing time,
- minimized dust,
- recyclability,
- smooth, sealed, and safe driving surface, and
- reduced tire-pavement noise generation.

Jahren et al. (2007) proposed a decision matrix to select an appropriate preservation treatment for different distress types and conditions, such as traffic volume and surface friction. As seen in Table 2.1, thin asphalt overlay was recommended in all distresses and conditions excluding the case of alligator cracking. It is noted that only seal coat was marginally recommended for the alligator cracking, while it was not applicable in heavy traffic.

Table 2.1 Decision matrix (Jahren et al. 2007)

Factor		Preservation Treatments				
		Fog seal	Seal coat	Slurry seal	Microsurfacing	Thin asphalt overlay (38.1mm)
Traffic volume	AADT<2,000 (low traffic)	R	R	R	R	R
	2,000>AADT>5,000 (medium traffic)	R	M	M	R	R
	AADT>5,000 (heavy traffic)	R	NR	NR	R	R
Bleeding		NR	R	R	R	R
Rutting		NR	NR	R	R	R
Raveling		R	R	R	R	R
Cracking	Few tight cracks	R	R	R	R	R
	Extensive cracks	NR	R	NR	NR	R
	Alligator cracking	NR	M	NR	NR	NR
Low friction		I	I	I	I	I

R=Recommended NR=Not Recommended M=Marginally Recommended I=May Improve
 AADT: Annual Average Daily Traffic

Brown and Heitzman (2013) evaluated several pavement preservation techniques, including crack treatment, fog seals, cheap seals, microsurfacing, slurry seals, and thin asphalt overlay. As shown in Figure 2.1, initial costs, expected extended life of pavement, and an annualized cost were investigated based on responses to the Federal Highway Administration (FHWA) from five selected states. Although crack treatment, fog seals, and chip seals had lower annualized costs than thin asphalt overlay, they could only provide limited benefits such as filling out cracking and/or sealing a cracked surface layer. On the other hand, thin asphalt overlay can correct rutting and improve smoothness and friction with long expected pavement life extension and inexpensive annualized cost.

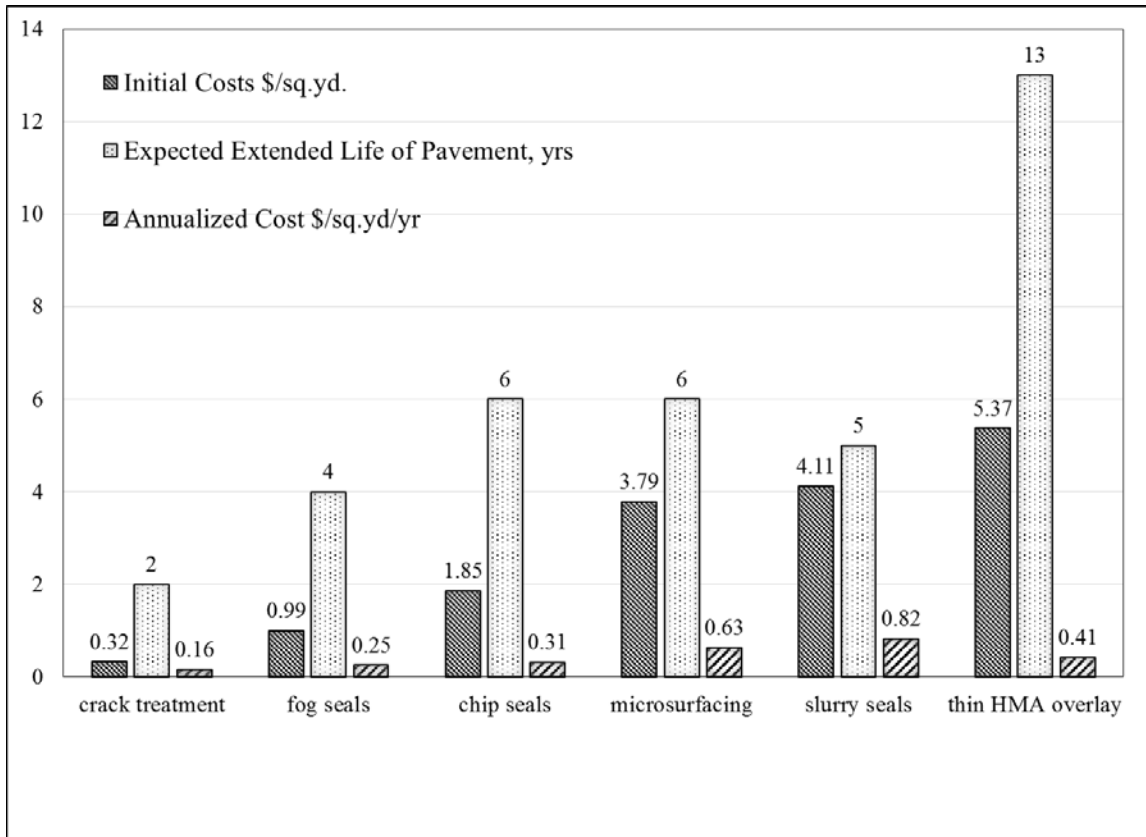


Figure 2.1 Typical unit costs and pavement life for specific maintenance and preservation treatments (Brown and Heitzman 2013)

2.2 Specifications of Thin Asphalt Overlay Materials, Mixtures, and Structures

2.2.1 Aggregate

The thickness of thin asphalt overlays are associated with NMAAS. In order to ensure adequate compaction, the overlay thickness to NMAAS ratio should be maintained in the range of 3:1 to 5:1 (Brown et al. 2004). Given the fact that the thickness of thin asphalt overlays is generally less than 38.1 mm (1.5 inches), NMAAS must be 12.5 mm or less. As shown in Table 2.2, most states used aggregates with NMAAS of 4.75 mm to 12.5 mm for thin asphalt overlays.

Table 2.2 NMAS requirements for a variety of states

State (mixture)	NMAS (mm)
Nebraska (SLX), Nevada, Utah, Mississippi (Mix 1), Massachusetts, Indiana, Missouri, Michigan	9.5
Alabama, North Carolina, Ohio (Type B)	12.5
New York, Maryland	6.3
Georgia, Mississippi (Mix 2), Ohio (Type A)	4.75

NMAS: Nominal Maximum Aggregate Size

The quality of aggregates was also specified by states based on predicted traffic, vehicle speed, and the type of overlaid pavement, as summarized in Table 2.3. Durability in terms of Los Angeles abrasion and sulfate soundness, as well as aggregate angularity and shape in terms of the number of fractured faces, is commonly checked for coarse aggregates (Newcomb 2009). For fine aggregates measures of cleanliness, such as sand equivalent values, are typically measured and specified (Newcomb 2009).

Table 2.3 Aggregate quality requirements for a variety of states

State	Los Angles Abrasion, % loss	Sulfate Soundness, % loss	2 or More Fractured Faces, %	1 Fractured Face, %	Sand Equivalent % (FA)	Uncompacted Void Content, % (FA)
Alabama	48	10	-	-	-	45
Maryland	-	-	-	-	-	40
Michigan	40	-	95	95	-	-
Nevada	37	12	80	90	-	-
New York	-	-	-	-	45	43
North Carolina	35	15	85	100	45	40
Ohio	40	12	-	100	-	-
Texas	30	20	95	-	45	-
Utah	40	16	90	-	45	-

FA: Fine Aggregate

2.2.2 Binder

To select an appropriate performance grade (PG) binder, temperatures and equivalent single axle loads (ESAL) were considered. As seen in Table 2.4, different states used various types of binders. Nebraska specifies PG 64-34 in its thin lift overlay mixtures (NDOR 2013), while Georgia, Missouri, and Virginia specify PG 64-22 (Newcomb 2009; Ahmed et al. 2013; Druta et al. 2013). Modified binders are used by Alabama, Florida, Michigan, New York, and Ohio (NYDOT 2008; Newcomb 2009).

Table 2.4 Comparative listing of bitumen in different states

State	PG	State	PG
Nebraska	64-34	Mississippi	76-22
Alabama	76-22 M*	Missouri	64-22
California	Depend on Climatic Region	New Jersey	76-22
Florida	67-22, 76-22 M	New York	64-22 M, 76-22 M
Georgia	64-22	North Carolina	76-22 for high ESAL [§] 64-22 for low ESAL
Indiana	70-28		
Iowa	70-22, 64-22	Ohio	76-22 M
Massachusetts	52-28	Texas	70-22, 76-22
Michigan	64-28 M, 70-22 M	Virginia	64-22

* Modified Binder

[§] Equivalent Single Axle Loads

2.2.3 Volumetric mix design

To meet structural and functional requirements of thin asphalt overlay, mix design specifications were designated. As shown in Table 2.5, N_{design} , air voids, voids in mineral aggregate (VMA), voids filled with asphalt (VFA), and asphalt content were specified by different states (Newcomb 2009, NDOR 2013). It is noted that only Ohio used the Marshall method to design thin lift mixture, while the rest of states designed the mixture using Superpave mix design.

Table 2.5 Mix design requirements in different states

State	N _{design}	Design Air Voids	VMA* (%)	VFA [§] (%)	Asphalt Content (%)
Nebraska (SLX)	50	4	16	-	5.3
Alabama	60	-	15.5	-	5.5
Georgia	50	4-7	-	50-80	6-7.5
Maryland	65	4	-	-	5-8
Massachusetts	75	4	15	65-78	-
Michigan	-	4.5-5	15.5	-	-
Mississippi	50-75	4-5.5	16-19	-	6.1
Nevada	-	3-6	12-22	-	-
New York	75	4	16	70-78	-
North Carolina	-	-		-	4.6- 5.6
Ohio	50-75	3.5	15	-	6.4
Texas	50	-	16	-	6.8-8
Utah	50-125	3.5	-	70-80	-

* Voids in Mineral Aggregate

[§] Voids Filled with Asphalt

2.2.4 Thin asphalt overlay thickness and its service life

Thin asphalt overlays with a thickness range of 15.8 mm to 50.8 mm (0.625 inch to 2 inches) have been used nationally and internationally, as seen in Table 2.6. It was reported that the expected extended service life was about 5 to 16 years (Newcomb 2009; Walubita and Scullion 2008; Watters 2006).

Table 2.6 Comparative thickness and service life in different states and countries

US States (mixture)	Thickness, mm	Expected service life, years
Nebraska (SLX)	25.4	-
Alabama	25.4-50.8	-
Arizona	25.4-38.1	-
California	30.4	-
Georgia	< 25.4	10
Illinois	31.8-38.1	7-10
Indiana	19	9-11
Maryland	19-25.4	-
Michigan	< 25.4	-
Minnesota	19-38.1	-
Mississippi	19-25.4	-
Missouri	45	-
New York	-	5-8
Ohio (Type A)	15.8-28.5	16
Ohio (Type B)	19-38.1	
Texas	25.4	
International Countries	Thickness, mm	Expected service life, years
Austria	20	10
Canada	20-40	8
New Zealand	12.7-30.4	-
United Kingdom	20.3-40.6	10-15

2.3 Laboratory Performance Tests

As seen in Table 2.7, some states and countries conducted different laboratory tests to evaluate the mixtures used in thin asphalt overlay and to predict pavement distresses such as rutting, cracking, and moisture-induced damage. Walubita and Scullion (2008) and Scullion et al. (2009) evaluated various thin asphalt overlay mixes to determine if they could guarantee adequate resistance to both rutting and cracking when subjected to different traffic and environmental conditions. The Hamburg wheel tracking test and overlay test were used to assess rutting and cracking potential. It was found that fine-graded mixtures with a 9.5 mm NMA

aggregate gradation predominantly consisting of Type F rock and screenings, and an asphalt binder content of over 7 percent was a promising candidate mix for use of thin overlay asphalt mixes.

Powell and Buchanan (2012) used the Asphalt Pavement Analyzer (APA) to assess the rutting potential of mixtures with different NMAAS (4.75, 9.5, and 12.5 mm) for thin asphalt overlays. It was concluded that the performance of the 4.75 mm NMAAS thin asphalt overlays was comparable to that of thin asphalt overlays with 9.5 and 12.5 mm NMAAS.

Mogawer et al. (2013) collected plant-produced mixtures from each thin asphalt overlay trial field in Minnesota, New Hampshire, and Vermont, and conducted a series of laboratory tests to measure mixture stiffness, moisture susceptibility, rutting potential, and cracking resistance. It was concluded that all mixtures had a high resistance to cracking, including reflective cracking and low temperature cracking, but this resistance could be reduced by adding RAP into the mixtures. On the other hand, half of the mixtures did not meet the rutting specification criteria, but no mixtures have exhibited rutting in the field.

Table 2.7 Summary of the laboratory tests

State	Testing method	To identify	Reference
Alabama	<ul style="list-style-type: none"> Asphalt Pavement Analyzer 	<ul style="list-style-type: none"> Rutting 	Powell and Buchanan (2012)
MN*, NH [§] , VT [†]	<ul style="list-style-type: none"> Dynamic Modulus test Hamburg test Overlay Tester Asphalt Concrete Cracking Device Semi-Circular Bending test 	<ul style="list-style-type: none"> Mixture Stiffness Moisture Susceptibility Reflective Cracking Low Temperature Cracking Fatigue Cracking 	Mogawer et al. (2013)
Texas	<ul style="list-style-type: none"> Hamburg Wheel Tracking Overlay Tester 	<ul style="list-style-type: none"> Rutting Cracking 	Walubita and Scullion (2008) Scullion et al. (2009)
Virginia	<ul style="list-style-type: none"> Model mobile load simulator 	<ul style="list-style-type: none"> Rutting Fatigue 	Druta et al. (2014)
Country	Testing method	To identify	Reference
South Africa	<ul style="list-style-type: none"> Model Mobile Load Simulator Pendulum Friction 	<ul style="list-style-type: none"> Rutting Skid Resistance 	Pretorius et al. (2004)
Australia	<ul style="list-style-type: none"> Cantabro 	<ul style="list-style-type: none"> Durability Binder Film Thickness 	Walubita and Scullion (2008)
Unite Kingdom	<ul style="list-style-type: none"> Indirect Tensile Stiffness Modulus Dynamic Creep 	<ul style="list-style-type: none"> Mixture Stiffness 	Nicholls et al. (2002)

*MN: Minnesota

[§]NH: New Hampshire

[†]VT: Vermont

2.4 Pavement Performance Predictions

The Mechanistic-Empirical Pavement Design Guide (MEPDG) was mainly used to investigate the structural performance of pavement structures with asphalt concrete overlays, as summarized in Table 2.8. Overlays with a thickness over 50.8 mm (2 inches) were considered for MEPDG simulations, while pavement structures with 25.4 mm (1 inch) thin overlay were simulated in Louisiana. Rutting, cracking, and the International Roughness Index (IRI) were major predicted distresses using MEPDG.

Table 2.8 Summary of the studies using MEPDG for the performance prediction of overlays

State	Performance indicator	Overlay thickness (mm)	Reference
South Dakota	<ul style="list-style-type: none">• Longitudinal cracking• Fatigue cracking• Transverse cracking• Rutting• IRI	50.8-127.0	Hoerner et al. (2007)
Tennessee	<ul style="list-style-type: none">• Rutting• IRI	108.0-343.0	Zhou et al. (2013)
Louisiana	<ul style="list-style-type: none">• Rutting• Fatigue cracking• IRI	25.4-121.9	Wu et al. (2008)
Minnesota	<ul style="list-style-type: none">• Transverse cracking	50.8	Johanneck et al. (2011)
Utah	<ul style="list-style-type: none">• Rutting• Fatigue cracking• IRI	45.7-58.4	Guthrie and Butler (2011)
Washington	<ul style="list-style-type: none">• Rutting• Fatigue cracking• Reflective cracking	50.8	Khazanovich et al. (2013)
Alberta (Canada)	<ul style="list-style-type: none">• Rutting• Fatigue cracking• IRI	50.0-120.0	Norouzi et al. (2014)

IRI: International Roughness Index

Another structural performance analysis tool is finite element modeling, which, compared to MEPDG, can provide more flexibility in selecting geometries, boundary conditions, and choosing materials in the analysis. There were a few studies that used finite element modeling for evaluating asphalt overlay pavement structures. Baek and Al-Qadi (2009) investigated reflective cracking of HMA overlays using finite element models that consisted of a 57-mm-thick overlay over a 200-mm-thick joint plain concrete pavement. As shown in Figure 2.2,

cohesive elements were embedded over the transverse joints, where reflective cracking potentially occurred in HMA overlays.

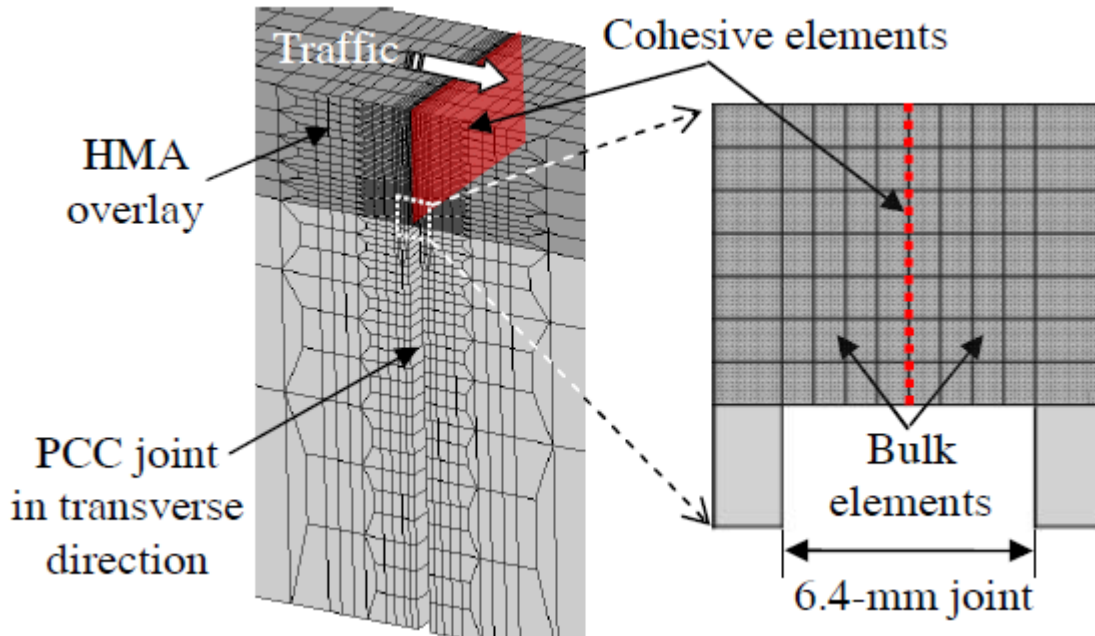
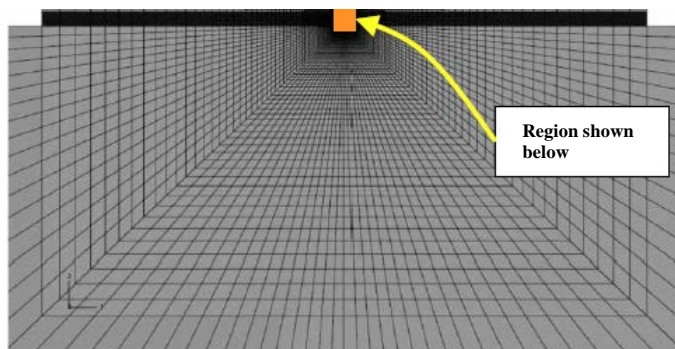
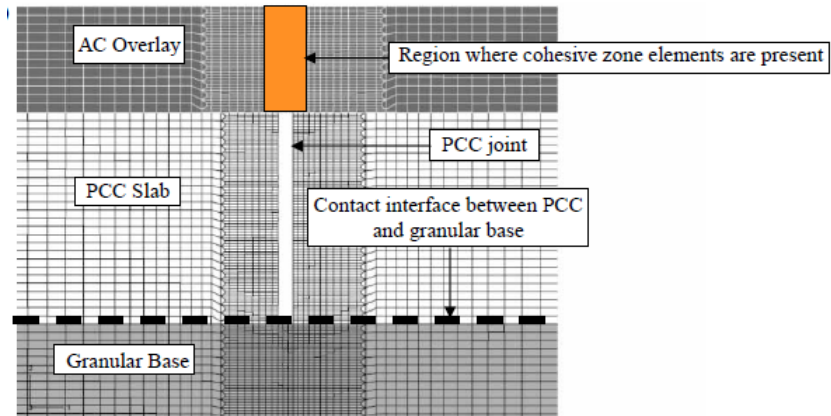


Figure 2.2 Reflective crack modeling in HMA overlay (Baek and Al-Qadi 2009)

Dave and Buttlar (2010) studied thermal reflective cracking of asphalt concrete overlays caused by a single, critical daily cooling event using finite element simulations and cohesive zone models, as shown in Figure 2.3. The type and thickness of overlays, joint/crack spacing, and the level of rubblization in the Portland cement concrete layer were varied to find several key material and pavement structure variables in the thermal reflective cracking mechanism.



(a) FE mesh showing the complete domain



(b) FE model details in the vicinity of the PCC joint

Figure 2.3 Finite element model (Dave and Buttlar 2010)

Ahmed et al. (2013) conducted finite element simulations to evaluate the structural performance of thin-bonded overlays. As shown in Figure 2.4, a thin overlay with 19 mm thickness and an old asphalt layer with 150 mm thickness were placed on granular base and soil subgrade in the finite element pavement model. Cohesive zone fracture elements were also employed to predict thermal and reflective cracking; the fracture properties for the model were obtained from a newly developed compact tension test.

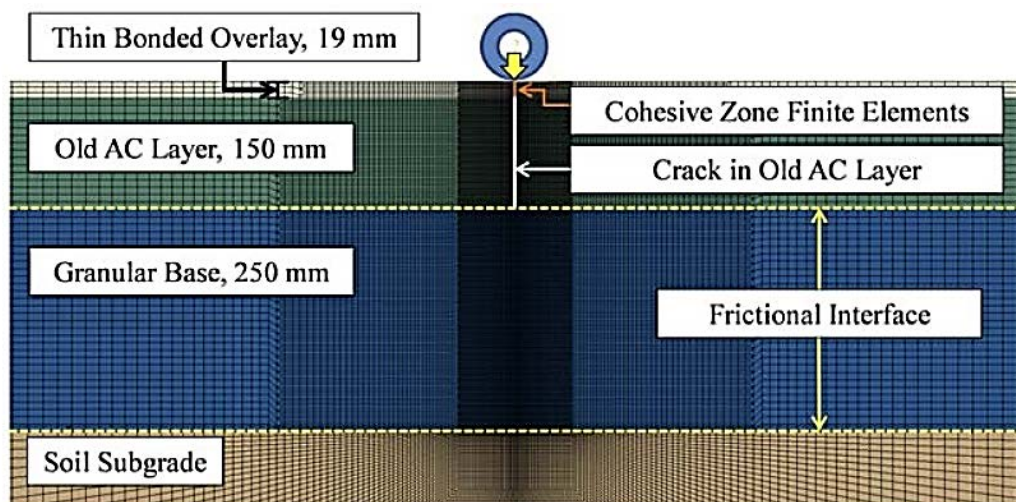


Figure 2.4 Finite element model (Ahmed et al. 2013)

Chapter 3 Material Selection and Sample Fabrication

This chapter describes the materials used and the sample fabrication process for this study. Two asphalt mixtures (SPH and SLX) paved during construction in July 2014 were collected and brought back to the laboratory. The asphalt mixtures were reheated to fabricate samples at the field compaction temperature.

3.1 Materials

Table 3.1 and Table 3.2 summarize the basic information on the SPH mixture and the SLX mixture, respectively, including percent of aggregates, aggregate gradation of the mixtures, and asphalt binder contents. Figure 3.1 shows the aggregate gradation of the mixtures and Figure 3.2 depicts the mixture microstructures. As shown in the aforementioned tables and figures, the SLX mix is composed of finer aggregates, with a nominal maximum aggregate size (NMAS) of 9.5mm, while the SPH mixture contains coarser aggregates with a NMAS of 12.5mm. Both mixtures were made of the same binder grade of PG 64-34. It should be noted that the amount of the virgin binder content added to the mixtures was 3.38% to the SPH mixture and 4.20% to the SLX mixture based on their recycled asphalt binder content.

Table 3.1 SPH mixture information

Material	% Agg.	Aggregate Gradation (% Passing on Each Sieve)									% Binder
		19mm	12.5mm	9.5mm	#4	#8	#16	#30	#50	#200	
¾"	10	100	60	18	2.0	2.0	1.0	1.0	1.0	1.0	5.2
CHIPS											
CR.	53	100	100	100	92.7	73	45.2	29.1	16.2	6.3	
Gravel											
2A	5	100	95.4	90.9	68	27.3	8.6	3.5	1.1	0.2	
Gravel											
Millings	32	100	94	90	68	41	29	23	19	8	
Combined		100	93.9	88.1	74.5	53.4	33.8	23.1	14.8	6	

Table 3.2 SLX mixture information

Material	% Agg.	Aggregate Gradation (% Passing on Each Sieve)									% Binder
		19mm	12.5mm	9.5mm	#4	#8	#16	#30	#50	#200	
3/8"	20	100	100	100	11.4	4.8	4.1	3.7	3.4	2.7	5.5
CHIPS											
CR.	50	100	100	100	92.7	73	45.2	29.1	16.2	6.3	
Gravel											
Millings	30	100	94	90	68	41	29	23	19	8.0	
Combined		100	98	97	69	49.8	32.1	22.2	14.5	6.1	

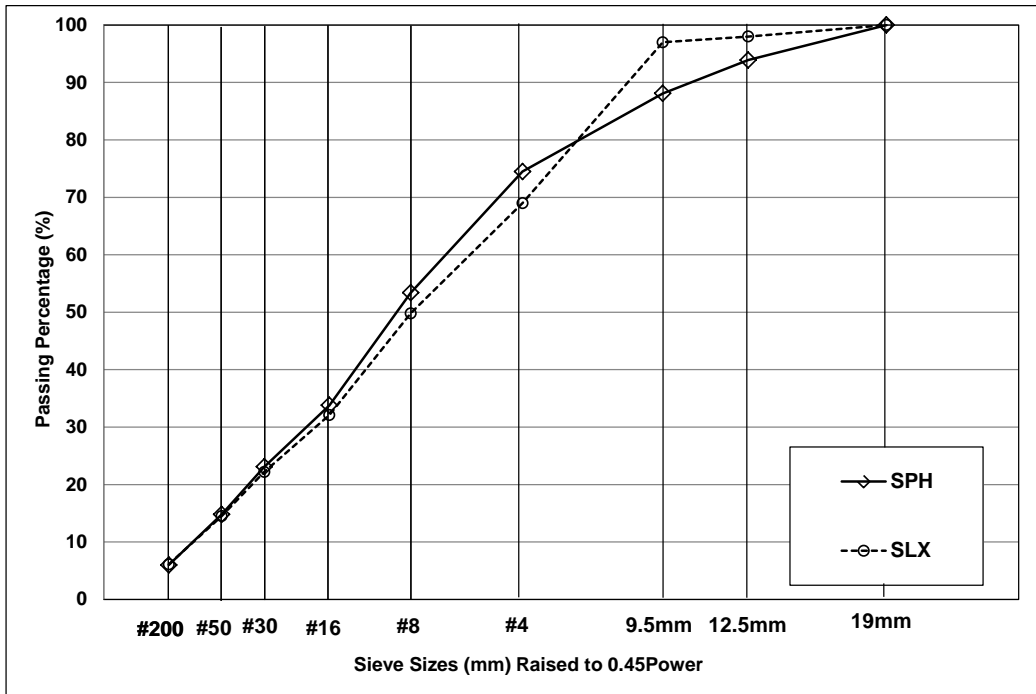


Figure 3.1 Aggregate gradation of the mixtures

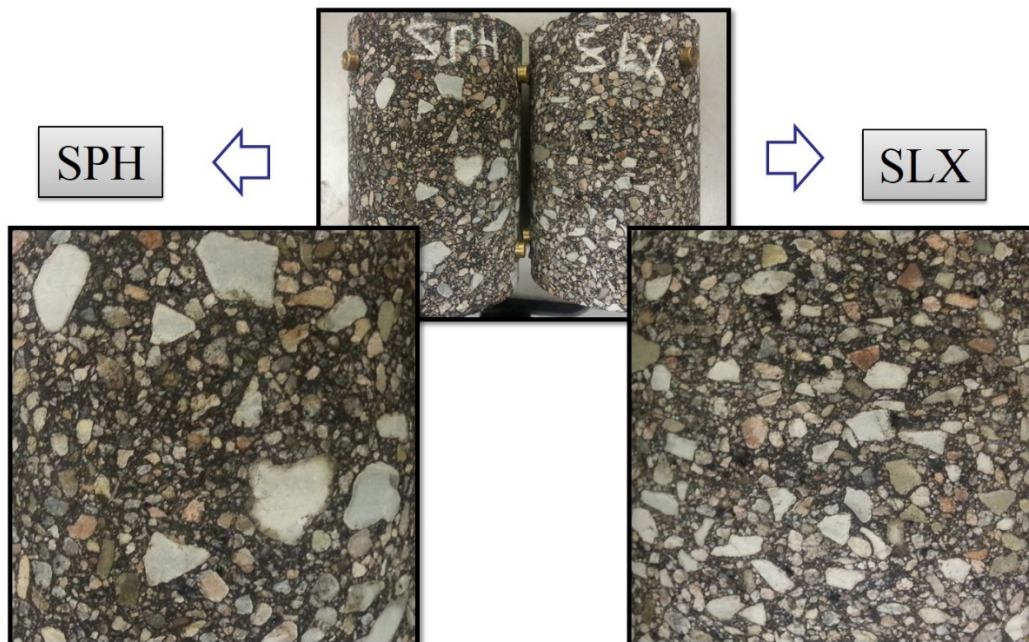


Figure 3.2 Picture of mixture microstructures

3.2 Specimen Fabrication

3.2.1 Dynamic modulus, dynamic creep, and static creep-recovery test specimens

As illustrated in Figure 3.3, the Superpave gyratory compactor was used to mold the cylindrical samples with a diameter of 150 mm and a height of 170 mm for the dynamic modulus, dynamic creep, and uniaxial static creep-recovery tests. The compacted samples were then cored and sawn to produce testing specimens targeting an air void of $4\% \pm 0.5\%$ with a diameter of 100 mm and a height of 150 mm. To measure the axial displacement of the specimen during the tests, epoxy glue was used to fix mounting studs to the surface of the specimen so that the three linear variable differential transformers (LVDTs) could be attached to the surface of the specimen at 120° radial intervals with a 70 or 100 mm gauge length. Next, the specimen was mounted into the testing station for testing.

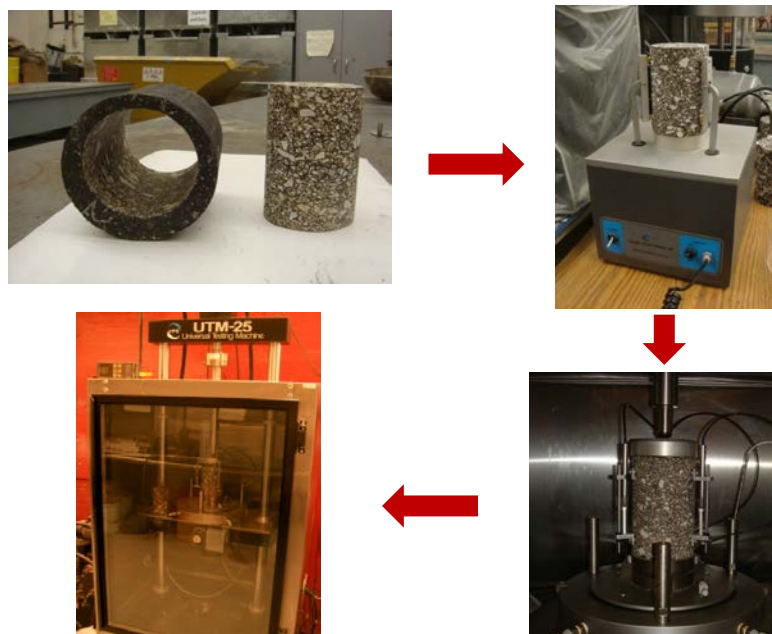


Figure 3.3 Specimen fabrication and uniaxial testing configuration

3.2.2 *Semi-circular bend fracture test specimens*

Figure 3.4 demonstrates the specimen production process and fracture testing configuration for the SCB fracture test. The Superpave gyratory compactor was used to produce tall compacted samples: 150 mm in diameter and 170 mm in height. Three slices (each with a diameter of 150 mm and a height of 50 mm) were obtained by removing the top and bottom parts of the tall sample. Finally, the slice was cut into two identical halves and the saw machine was used to make a vertical notch: 15 mm long and 2.5 mm wide.

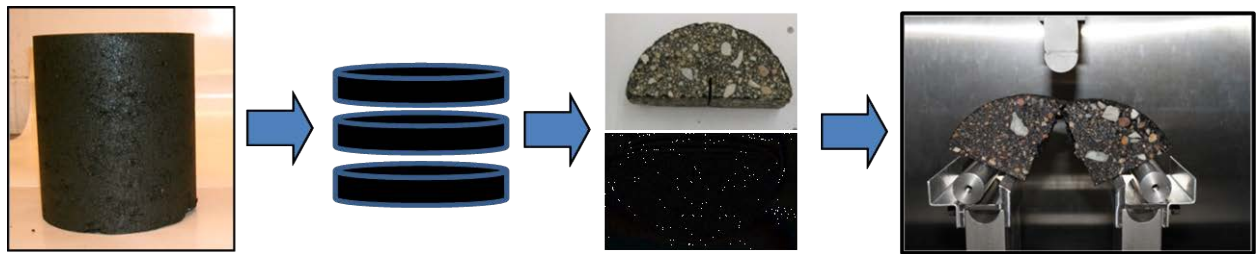


Figure 3.4 SCB specimen fabrication and fracture testing configuration

3.2.3 *Hamburg wheel tracking test specimens*

To fabricate Hamburg wheel tracking test (HWTT) specimens, a Superpave gyratory compactor was used to produce cylindrical specimens with a diameter of 150 mm and a height of 62 mm by targeting an air void of 7 percent \pm 0.5 percent. A masonry saw was used to cut along the edge of the cylindrical specimens. Then the specimens, which were fitted with high-density polyethylene molds, were placed in a stainless steel tray mounting system as shown in Figure 3.5.



(a) cut specimen after compaction



(b) cylindrical specimen mounting system

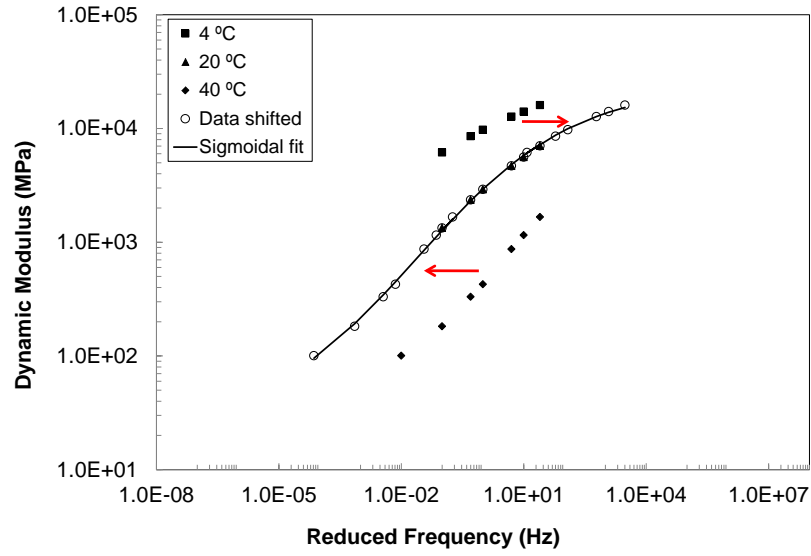
Figure 3.5 Hamburg wheel tracking test specimen sawn and mounting system

Chapter 4 Laboratory Tests and Data Analysis

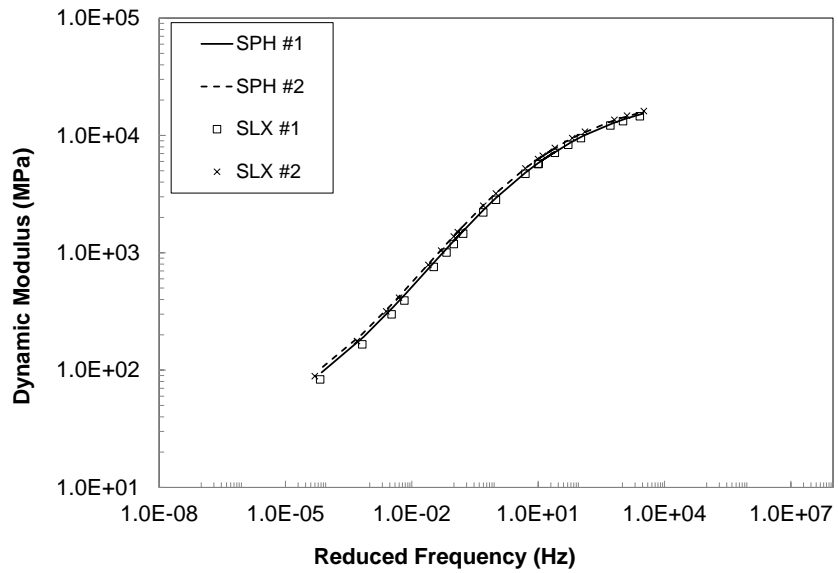
This chapter describes laboratory tests conducted for this study and test results. Various laboratory tests, including a dynamic modulus test, dynamic creep test, static creep-recovery test, SCB fracture test, and Hamburg wheel tracking test were performed to compare the performance behavior and to characterize material properties of asphalt mixtures (SPH vs. SLX).

4.1 Dynamic Modulus Test and Results

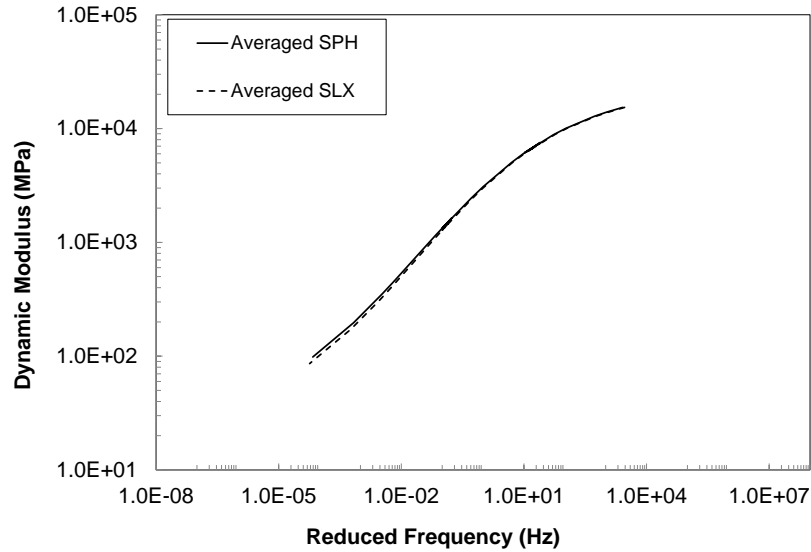
The dynamic modulus test was conducted to characterize the linear viscoelastic stiffness of the asphalt mixtures. The test was conducted using an asphalt mixture performance tester, also known as AMPT. The test procedure was following the AASHTO TP79 standard (AASHTO 2008; AASHTO 2011). Three temperatures of 4, 20, and 40 °C and six or seven loading frequencies of 25, 10, 5, 1, 0.5, and 0.1 Hz, and 0.01 Hz (40 °C only) were used, and the frequency-temperature superposition concept was applied to obtain the linear viscoelastic master curves at a target reference temperature of 20 °C. Two replicates were tested, which obtained the average values of dynamic modulus at each different testing temperature over the range of loading frequencies. For details, Figure 4.1 (a) shows an example of constructing a master curve for SPH specimen #1. Based on this process, each master curve of each tested specimen is developed, as shown in Figure 4.1 (b). Finally, average values of dynamic modulus are obtained and plotted in Figure 4.1 (c). As shown in Figure 4.1, the test results between the replicates were very repeatable and both mixtures showed very similar viscoelastic stiffness characteristics. The measured dynamic modulus of each mixture will be used for the MEPDG simulation and finite element pavement modeling.



(a) development of a master curve



(b) individual master curve



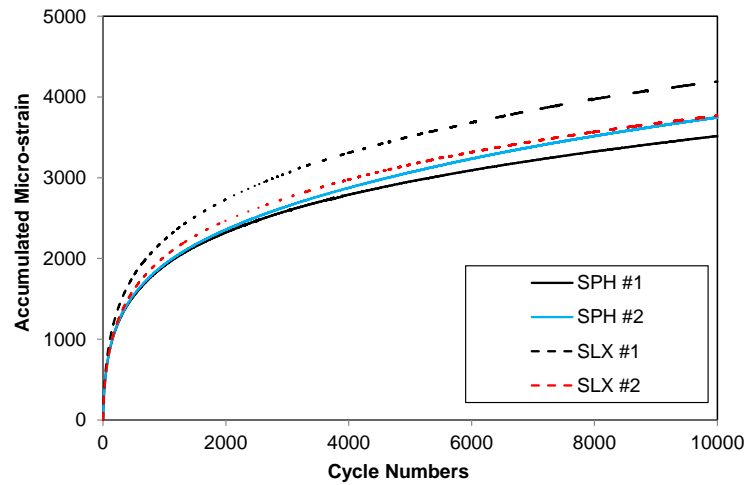
(c) averaged master curve for each mixture

Figure 4.1 Dynamic modulus test results

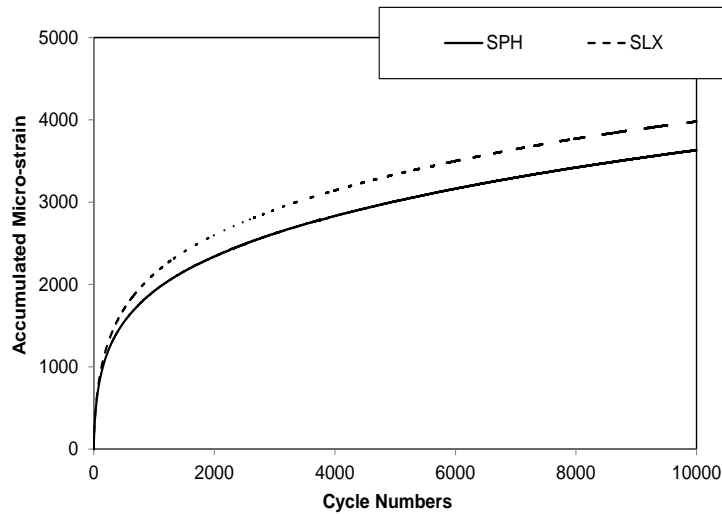
4.2 Dynamic Creep Test and Results

The dynamic creep test was conducted to compare the permanent deformation behavior of asphalt mixtures at 40°C. The specimens used for the dynamic modulus test were re-used and the test procedure followed the standard, AASHTO TP79 (AASHTO 2011). The unconfined and repeated loading was applied with a deviator stress level of 138kPa at 40°C. The loading stress was applied in the form of a haversine curve with a loading time of 0.1 second and a rest period of 0.9 second in one cycle. Loading stress was repeatedly applied to the specimens until they exhibited a tertiary flow and reached 5% permanent strain level or the number of loading cycles reached 10,000. Two replicates from each mixture were tested, and the results of which are presented in Figure 4.2. The test results between the replicates were repeatable without large discrepancies. The coefficient of variation for mean from both mixtures was less than 10%, which satisfies the range recommended by the standard. The measured accumulative permanent strain against the number of loading cycles of the SPH mixture was less than that of the SLX

mixture: the accumulative permanent strain measured at 10,000 cycle of the SPH mixture was approximately 9% lower than the SLX mixture. This implies that both mixtures will present similar rutting resistance at a 40 °C service temperature.



(a) individual



(b) average

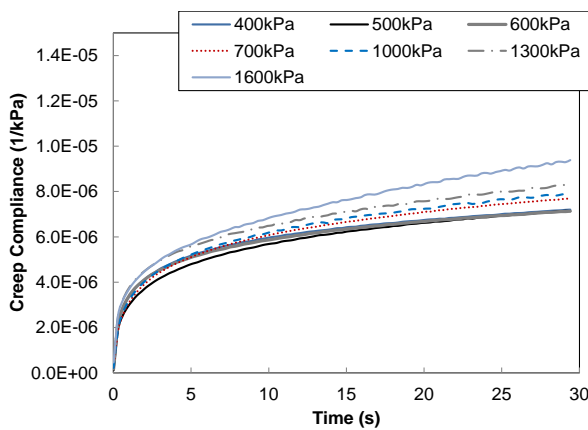
Figure 4.2 Dynamic creep test results

4.3 Static Creep-Recovery Test and Results

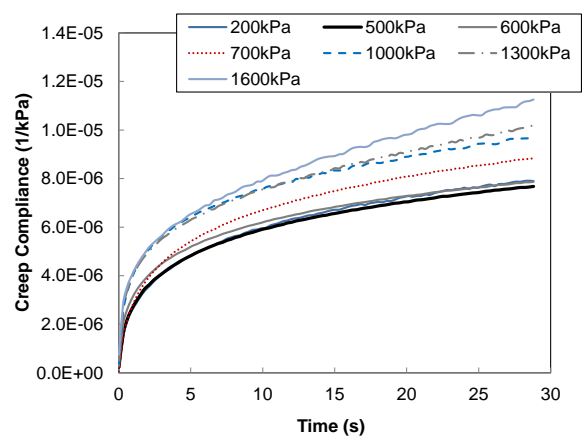
The static multiple-stress, creep-recovery test was conducted to identify the stress-dependent, nonlinear behavior of the asphalt mixtures. At a test temperature of 30°C, a creep stress was applied to the specimens for 30 s (followed by a 500-s recovery period), and the vertical displacement (in compression) was monitored with the three linear variable differential transducers. A large range of creep stresses was applied to identify the level of (stress-independent) linear viscoelastic range and to characterize the stress-dependent nonlinear behavior of each mixture. Static creep compliance, which defines a ratio of time-dependent strain to the applied static stress, was monitored over loading time to determine linear viscoelastic stress levels based on the homogeneity concept. In the theory of linear viscoelasticity, the homogeneity concept indicates that the ratio of strain response to any applied stress is independent of the magnitude of the stress. As illustrated in Figures 4.3 (a) and (b), preliminary tests with a large range of creep stresses indicated that both of the mixtures were linear viscoelastic up to 600 kPa in the uniaxial creep stress. In other words, nonlinear viscoelasticity began when the stress level was greater than about 600 kPa. Therefore, any creep-recovery curve within the linear viscoelastic range (600 kPa in this case) can be used to determine the linear viscoelastic properties. Other creep-recovery curves obtained from stress levels that were greater than the linear viscoelastic range can be used to characterize the stress-dependent nonlinear viscoelastic properties of each mixture. It should be noted that the characterization of these stress-dependent nonlinear viscoelastic properties of asphalt mixtures is not presented herein because it is outside the scope for this paper, but it is well described in other studies (Ban et al. 2013; Im et al. 2015). These stress-dependent nonlinear viscoelastic properties of asphalt mixtures can be used with finite element analyses (FEA) for further simulation of the pavement's

rutting performance. Any significant findings from the FEA simulation results will be presented in a later publication.

Figures 4.3 (c) and (d) present the results of multiple stress creep-recovery tests of each mixture. Each strain curve at a specific creep stress level was averaged from two or three replicates. Test results between replicates generally were similar, so the averaged curves presented in the figure were used to estimate the deformation characteristics of each mixture. As shown in the figure, higher stress levels generated greater creep strain and provided less recovery at the test temperature (30 °C). The SPH mixture exhibited a bit lower creep compliance or strain than those of the SLX mixture at the same stress levels. One interesting observation from these figures is that both mixtures showed similar deformation characteristics until the stress level of 600 kPa, which is the level of linear viscoelastic range, however, the strain difference between the two mixtures increased as the stress level increased, as demonstrated in Figures 4.3 (e) and (f). These results clearly indicate the stress level- and material-dependent characteristics of the two mixtures.



(a) creep compliance of SPH mixture



(b) creep compliance of SLX mixture

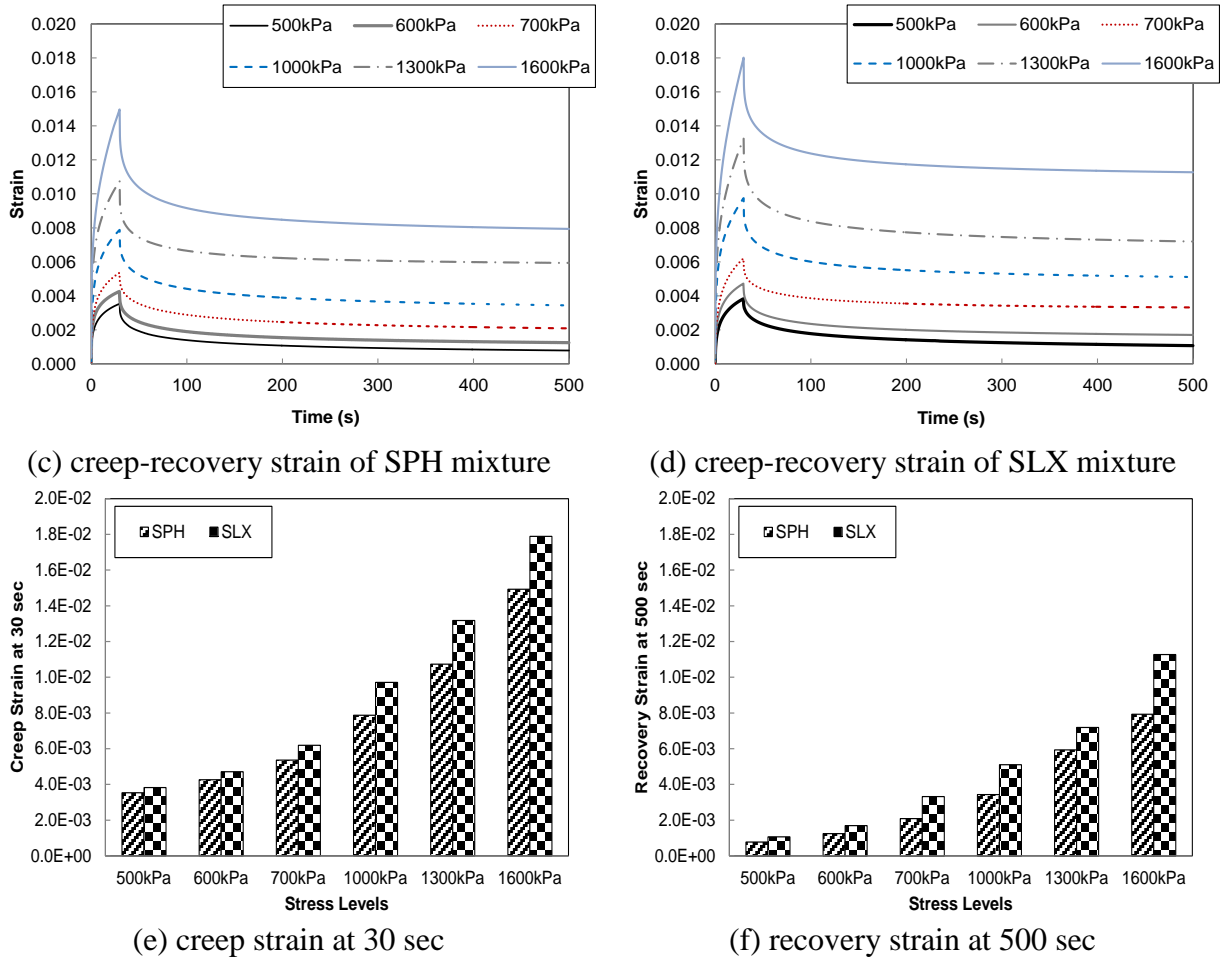


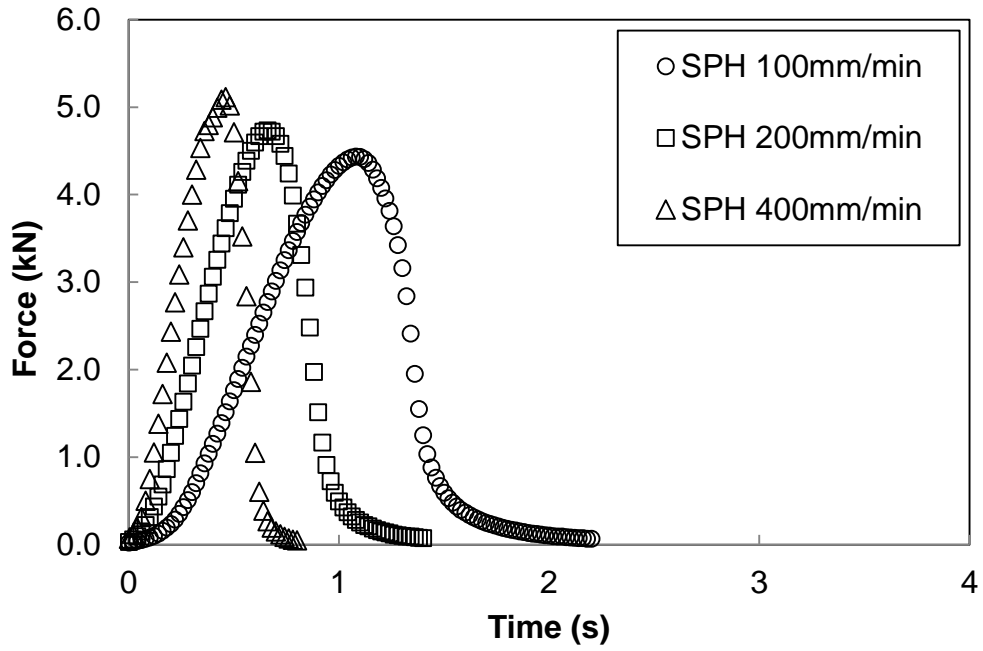
Figure 4.3. Repeated creep-recovery test results of each mixture

4.4 SCB Fracture Test and Results

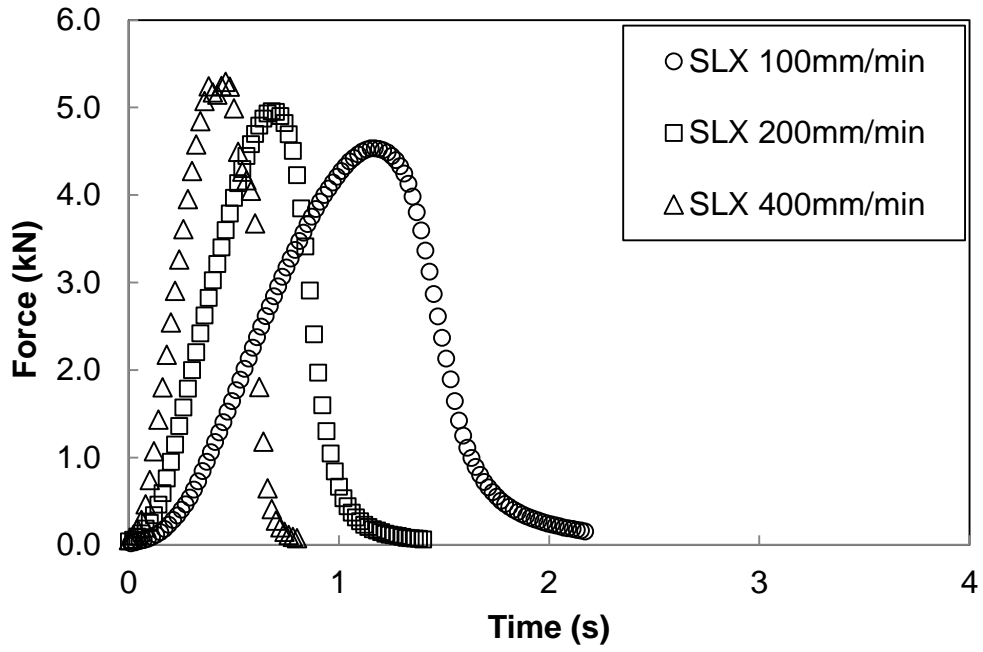
A total of nine SCB specimens were prepared for each mixture to complete three replicates per each test case. Prior to testing, individual SCB specimens were placed inside the environmental chamber of a mechanical testing machine for temperature equilibrium targeting the testing temperature of 21°C. Following the temperature conditioning step, specimens were subjected to a simple three-point bending configuration with three different monotonic displacement rates (i.e., 100, 200, and 400 mm/min.) applied to the top center line of the SCB specimens. As shown in Figure 3.4, metallic rollers separated by a distance of 122 mm (14 mm

from the edges of the specimen) were used to support the specimen. Reaction force at the loading point was monitored by the data acquisition system installed in the mechanical testing machine.

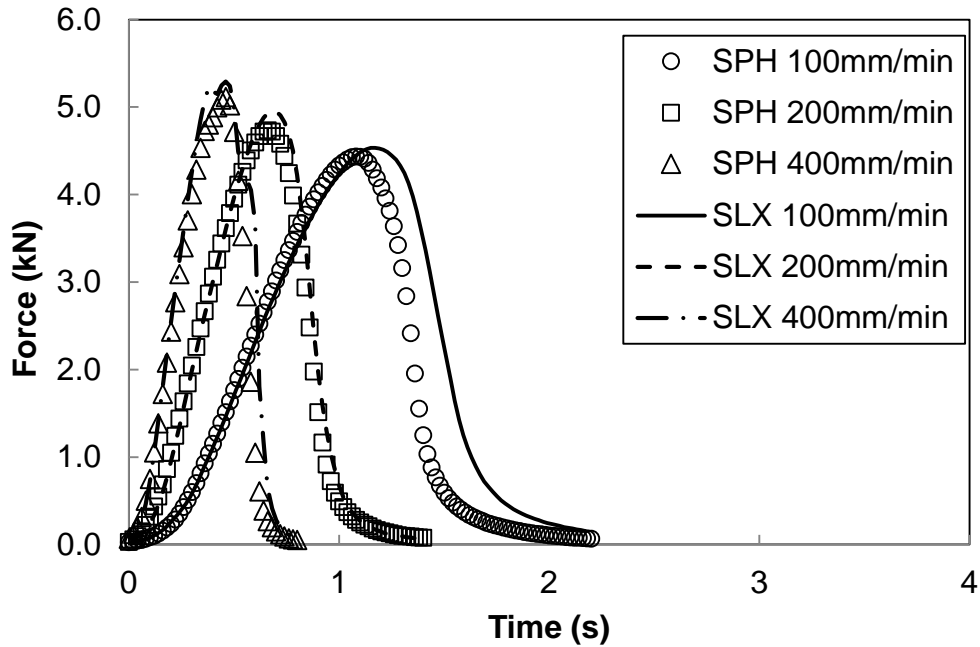
Figure 4.4 presents the SCB test results by plotting the reaction forces at the point of the load application as the loading time increases. The test results among the replicates were repeatable without large discrepancies. The coefficient of variation (COV) in the peak force for each loading case of the SPH mixture was between 11.1% and 15.6%, while the SLX was between 3.9% and 16.8%. The COV values obtained in this study were reasonable compared to a recent study that showed a range between 15% and 34 % (Marasteanu et al. 2007). As seen in Figure 4.4, the rate-dependent behavior was observed from both asphalt mixtures: the peak force slightly increases as the loading rate becomes higher. Also, the fracture behavior of both asphalt mixtures (SPH and SLX) was compared and exhibited similar fracture characteristics. The fracture properties of each mixture are then determined by means of the cohesive zone computational modeling of the SCB fracture test as presented in the following chapter.



(a) SPH mixture



(b) SLX mixture



(c) comparison between SPH mixture and SLX mixture (average)

Figure 4.4 SCB test results

4.5 Hamburg Wheel Tracking Test and Results

The Hamburg wheel tracking test was conducted at a temperature of 50 °C in accordance with AASHTO T 324, Hamburg Wheel-Track Testing of Compacted Hot Mix Asphalt (AASHTO 2011). To evaluate the rutting susceptibility and moisture resistance, specimens were submerged under water at a temperature of 50 °C during the test, and a LVDT device measured deformations. The stop criterion was rut depth of 12.5 mm or 20,000 passes. Figure 4.5 shows images of HWTT specimens after testing. The test results are summarized in Table 4.1 and the rut depth result of each mix from the second round test is plotted in Figure 4.6. As shown, the SPH mixture provided satisfactory performance while the SLX did not. This might be because the SPH mixture contained coarser aggregates, with the NMAS of 12.5 mm, than those of the SLX, with a NMAS of 9.5 mm. However, it should be noted that the Hamburg wheel tracking

test applies somewhat unrealistic (harsh loading-environment) conditions that may not represent actual field performance of mixture moisture damage. With respect to stripping, a stripping inflection point (SIP) was determined based on the standard method as shown in Figure 4.6. As shown, the SIP of the SLX mixture was around 12,000, while that of the SPH was not determined since stripping did not occur during the test. However, from the visual observation seen in Figure 4.5 (b), both mixtures did not show much difference in the degree of stripping.



(a) typical image after testing



(b) a closer look for stripping observation

Figure 4.5 Images of Hamburg wheel tracking test specimens after testing

Table 4.1 Summary of Hamburg wheel tracking test results of each mixture

1st. Round Test			
Number of Passes	Rut Depth (mm)		Number of Passes
	SPH	SLX	
5,000	-2.27	-3.48	5,000
10,000	-2.69	-5.25	10,000
15,000	-3.41	-11.55	15,000
20,000 (Pass)	-4.38	-12.59	15,400 (Fail)
2nd. Round Test			
5,000	-2.54	-3.47	5,000
10,000	-3.18	-5.66	10,000
15,000	-4.00	-11.38	15,000
20,000 (Pass)	-4.80	-12.05	15,300 (Fail)

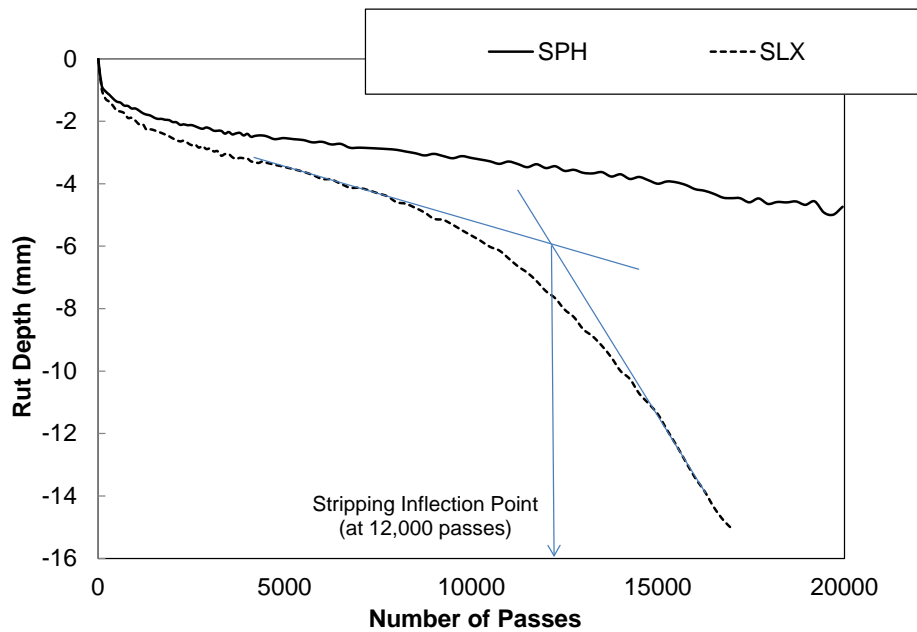


Figure 4.6 Plot of Hamburg wheel tracking test results of each mixture

Chapter 5 Characterization of Material Properties

In this chapter the dynamic modulus test, static multiple stress creep-recovery test, and SCB fracture test results presented in the previous chapter are used to characterize material properties for computational pavement performance simulation. Using dynamic modulus test results, viscoelastic properties such as Prony series coefficients and time-temperature shift factors were identified and static multiple stress creep-recovery test results were used to obtain viscoplastic parameters for rutting simulation. Fracture properties for cracking simulation were also determined from the SCB test results. This chapter contains a brief explanation on characterizing material properties. More details on the model used to characterize the material properties and identification process is presented in Appendix A.

5.1 Viscoelastic Material Properties

A three-dimensional representation of Schapery's nonlinear viscoelastic single-integral constitutive model (Schapery 1969) can be expressed as (Lai and Bakker 1996):

$$\begin{aligned} \varepsilon_{ij}^{ve}(t) = & \frac{1}{2} J_0 g_0 \bar{s}_{ij}(t) + \frac{1}{2} g_1 \int_0^t \Delta J^{(\psi' - \psi^\zeta)} \frac{d(g_2 \bar{s}_{ij}(\zeta))}{d\zeta} d\zeta \\ & + \frac{1}{9} B_0 g_0 \delta_{ij} \bar{\sigma}_{kk}(t) + \frac{1}{9} \delta_{ij} g_1 \int_0^t \Delta B^{(\psi' - \psi^\zeta)} \frac{d(g_2 \bar{\sigma}_{kk}(\zeta))}{d\zeta} d\zeta \end{aligned} \quad (5-1)$$

Viscoelastic material parameters were obtained using equation (5-1). Details are given in the Appendix A subsection: A.1 Viscoelastic Material Properties. By minimizing the error between the dynamic modulus test results and Prony series equations, the coefficients D_n and λ_n are obtained and summarized in Table 5.1.

Table 5.1 Obtained viscoelastic properties

Time-temperature shift factors					
SPH			SLX		
Temperature (°C)	a_T		Temperature (°C)	a_T	
4	2.184		4	2.232	
21	1.000		21	1.000	
40	0.009		40	0.007	
Prony series coefficients					
SPH			SLX		
n	$\lambda_n(\text{s}^{-1})$	$D_n(\text{MPa}^{-1})$	n	$\lambda_n(\text{s}^{-1})$	$D_n(\text{MPa}^{-1})$
0	-	6.69×10^{-5}	0	-	7.24×10^{-5}
1	1.41×10^4	2.85×10^{-5}	1	1.04×10^4	3.08×10^{-5}
2	1.84×10^3	3.24×10^{-5}	2	1.37×10^3	3.34×10^{-5}
3	2.40×10^2	6.31×10^{-5}	3	1.80×10^2	7.04×10^{-5}
4	3.13×10^1	1.30×10^{-4}	4	2.37×10^1	1.46×10^{-4}
5	4.08×10^0	2.52×10^{-4}	5	3.12×10^0	2.95×10^{-4}
6	5.32×10^{-1}	5.21×10^{-4}	6	4.10×10^{-1}	6.20×10^{-4}
7	6.94×10^{-2}	1.76×10^{-3}	7	5.39×10^{-2}	2.11×10^{-3}
8	9.05×10^{-3}	3.30×10^{-3}	8	7.09×10^{-3}	3.90×10^{-3}
9	1.18×10^{-3}	8.11×10^{-3}	9	9.33×10^{-4}	9.17×10^{-3}

5.2 Viscoplastic Material Properties

The viscoplastic strain was extracted by subtracting the viscoelastic strain from the total strain that was obtained from the static multiple stress creep-recovery test. To characterize the viscoplastic deformation of each mixture, the following viscoplastic flow rule proposed by Perzyna (1971) was used in this study:

$$\dot{\epsilon}_{ij}^{vp} = \Gamma^{vp} \left\langle \frac{f}{\sigma_y^0} \right\rangle^N \frac{\partial g}{\partial \bar{\sigma}_{ij}} \quad (5-2)$$

Viscoplastic properties were identified by equation (5-2). Details are given in the Appendix A subsection: A.2 Viscoplastic Material Properties. As presented in Figure 5.1 and summarized in Table 5.2, a similar hardening response of SPH and SLX was observed. This implies that SLX had similar rutting potentials to SPH, which agreed with the static creep-recovery test results presented in Chapter 4.

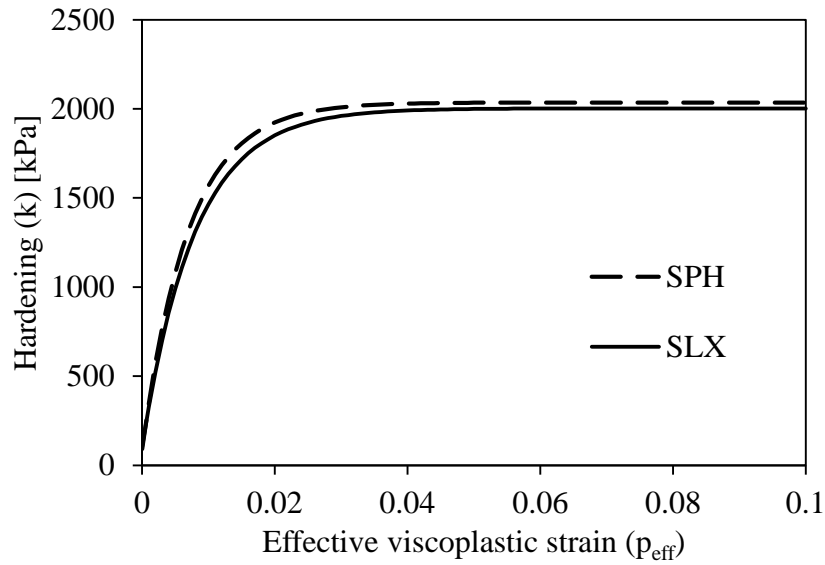


Figure 5.1 Hardening response of SPH and SLX

Table 5.2 Identified viscoplastic material properties ($T_{ref}=21^{\circ}\text{C}$)

	$\Gamma_0^{vp}(1/s)$	N	$k_0(\text{kPa})$	$k_1(\text{kPa})$	k_2
SLX	5.80×10^{-5}	1.40	98.84	1903.85	126.52
SPH	4.15×10^{-5}	1.23	90.71	1945.15	142.54

5.3 Fracture Properties

The cohesive zone fracture energy (Γ_c), which is the locally estimated fracture toughness, can then be quantified by computing the area below the bilinear traction-separation curve with peak traction (T_{\max}) and critical displacement (δ_c) as follows:

$$\Gamma_c = \frac{1}{2} \delta_c T_{\max} \quad (5-3)$$

As detailed in the Appendix A subsection: [A.3 Fracture Properties](#), the fracture properties in the bilinear cohesive zone model, T_{\max} and Γ_c were determined for each case through the calibration process until a good match between the SCB test results and their computational simulations was observed. The identified fracture properties for different loading rates are summarized in Table 5.3. The good agreement between tests and model simulations indicates that the local fracture properties were properly defined through the integrated experimental-computational approach. From the table, it is clearly seen that the fracture properties of SLX are similar to those of SPH, implying that the cracking resistance of SLX is not quite different from that of SPH.

Table 5.3 Cohesive zone fracture properties

Loading rate (mm/min.)	Fracture properties	Mix type	
		SPH	SLX
100	T_{\max} (MPa)	7.45	7.50
	Γ_c (J/m ²)	2950	3000
200	T_{\max} (MPa)	7.95	8.00
	Γ_c (J/m ²)	3450	3500
400	T_{\max} (MPa)	7.75	8.00
	Γ_c (J/m ²)	4800	5000

5.4 Viscodamage Material Properties

In order to simulate pavement fatigue cracking, continuum damage mechanics was employed in this study. As detailed in the Appendix A subsection: A.4 Viscodamage Material Properties, the damage density (ϕ) has a range from 0 to 1, where $\phi = 0$ means that the material is intact, while $\phi = 1$ means that the material is fully damaged. The damage density can be calculated by nominal (damaged) stress (σ) and effective (undamaged) stress ($\bar{\sigma}$). The nominal stress was measured from a cohesive element located in a crack-tip (see Figure A.2) during the SCB test simulation with the fracture properties obtained above. The effective stress was calculated from an element in the same location during the SCB test without considering fracture of the material. Using the thermo-viscodamage evolution law proposed by Darabi et al. (2013), the viscodamage parameters were obtained, as summarized in Table 5.4.

Table 5.4 Viscodamage material properties ($T_{ref} = 21^\circ\text{C}$)

SPH				SLX			
Γ^{vd}	q	k	$Y_0(\text{kPa})$	Γ^{vd}	q	k	$Y_0(\text{kPa})$
8.55×10^{-17}	4.85	-2.40	1000	2.86×10^{-18}	5.51	-2.45	1000

Chapter 6 Pavement Performance Predictions

NDOR paved two different overlays (i.e., SLX and SPH) from I-80 Exit 279 near Kearney, Nebraska in 2014, as seen in Figure 6.1 and Figure 6.2. Layer configurations for both overlays are presented in Figure 6.3. Based on that information, this chapter compares the structural behaviors of the two overlays using SLX and SPH through the Mechanistic-Empirical Pavement Design Guide (MEPDG), life cycle cost analysis (LCCA), and finite element modeling.



Figure 6.1 Project location: I-80 Exit 279 near Kearney, Nebraska

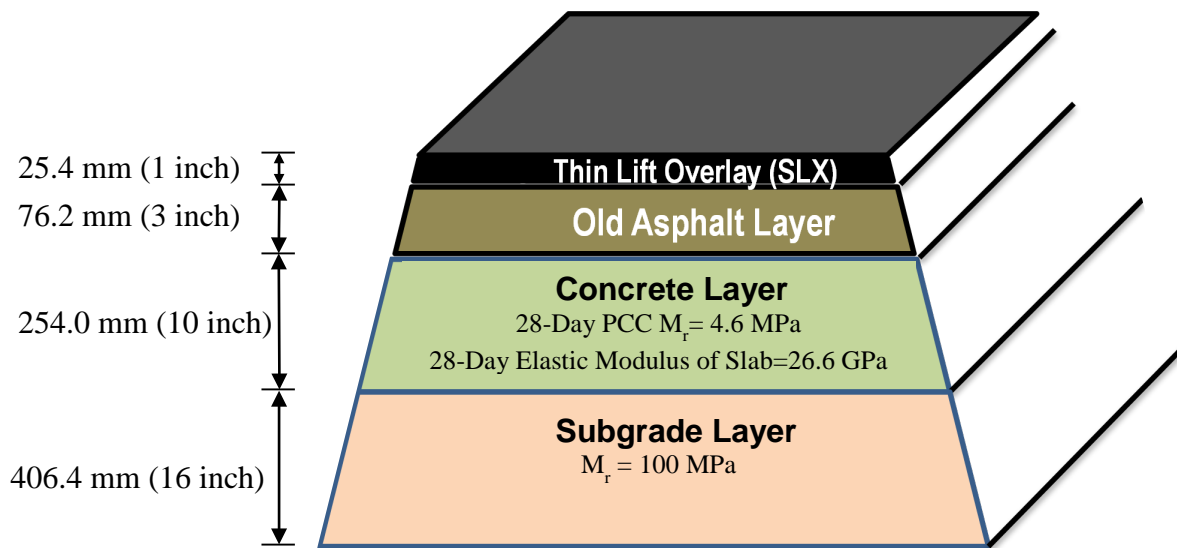


(a) old asphalt layer milled

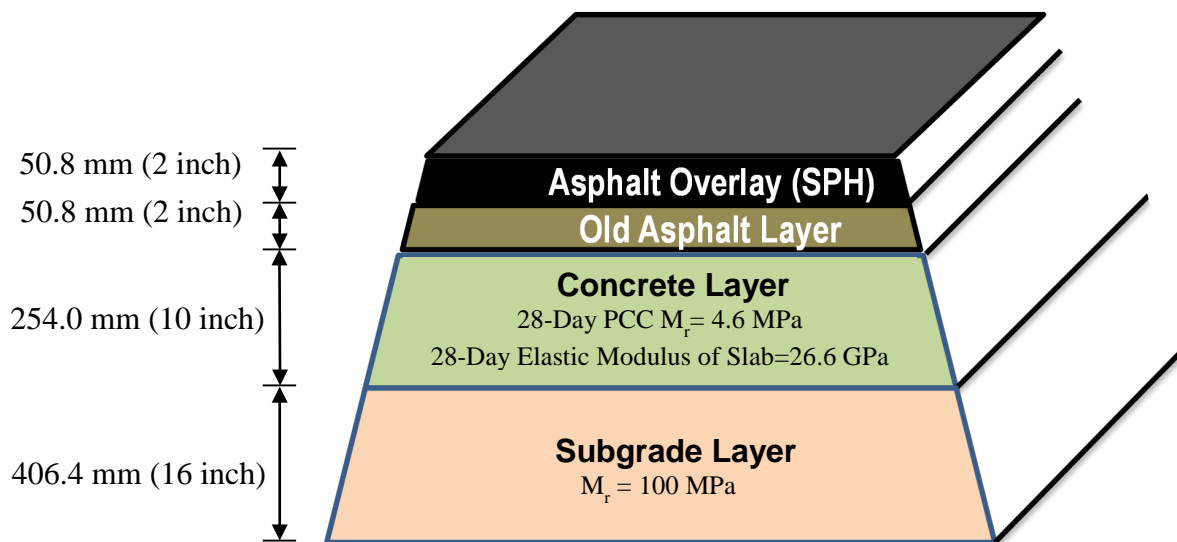


(b) new overlay paved

Figure 6.2 Pavement construction



(a) SLX pavement structure



(b) SPH pavement structure

Figure 6.3 Layer configuration of two pavement structures

6.1 MEPDG Simulation

MEPDG was used to evaluate the structural performance of the pavements overlaid with SLX or SPH. Table 6.1 summarizes the design input parameters for the simulations and presents simulation results. A 15-year design period with a vehicle operation speed of 60 mph was selected for simulations with a 90% design reliability level. Default values were used for most inputs related to traffic, except for an average annual daily truck traffic (AADTT) of 8,891 that was provided by NDOR. For climate inputs, the location of project site was assumed to be Lincoln, Nebraska. As shown, most of the inputs for MEPDG simulations were similar for both pavement structures, while the type of overlay, the thickness of the overlay, and the old asphalt layer were different. The results of the dynamic modulus test of each mixture were used for the SLX and SPH overlays, while the material properties of other layers (i.e., viscoelastic properties of the old asphalt layer, mean elastic modulus of concrete layer, and resilient modulus of subgrade) were obtained from a previous study (Im et al. 2010).

Table 6.1 presents MEPDG predictions of two distresses (cracking and rutting). As shown, cracking was not a serious issue for both pavement structures during the 15-year design period. However, the SLX pavement was more susceptible to longitudinal cracking, which did not agree with the laboratory SCB test results presented in Figure 4.5 and Table 5.3. This was because the results of the dynamic modulus test are major inputs in the predictive cracking model in the MEPDG. MEPDG simulation results of cracking require further investigation due to limited predicting power of crack-associated damage behavior. With respect to rutting, the simulation results indicated that the pavement with SLX did not satisfy the rutting criterion, while serious distresses did not occur in the SPH pavement during the design period. However, the rutting in the SLX pavement structure may not be critical because the predicted permanent

deformation passed over the rutting design limit in about 13 years after its construction. It is noted that the expected service life of thin asphalt overlays is typically 5-15 years (Walubita and Scullion 2008).

Table 6.1 Summary of key inputs of MEPDG simulations and results

Design Period (year)	15			
Operation Speed (mph)	60			
Design Reliability (%)	90			
Initial two-way AADTT	8,891			
Project Location	Lincoln, NE			
Performance Criteria	<ul style="list-style-type: none"> • Initial IRI (in/mile): 63 • Terminal IRI (in/mile): 172 • AC surface down cracking (ft/mile): 1,000 • AC bottom up cracking (%): 25 • AC thermal cracking (ft/mile): 1,000 • AC Permanent deformation (in): 0.25 • Total permanent deformation (in): 0.75 			
MEPDG simulation results				
	SLX structure		SPH Structure	
Performance Criteria	Distress Predicted	Reliability Predicted	Distress Predicted	Reliability Predicted
Long. Cracking (ft/mile)	7	92.03 (Pass)	0	99.99 (Pass)
Bottom Up Cracking (%)	0	99.99 (Pass)	0	99.99 (Pass)
Rutting (AC Only) (in):	0.27	40.01 (Fail)	0.11	99.99 (Pass)

6.2 Life Cycle Cost Analysis (LCCA) and Results

The life cycle cost analysis (LCCA) of each pavement structure was conducted to investigate the economic benefits of the thin-lift overlay practice compared to the two-inch rehabilitation. An LCCA tool developed by the Federal Highway Administration (FHWA), called RealCost 2.5 (FHWA 2010), was used in this study.

Major inputs, the activities of each alternative, and assumptions made for the LCCA are summarized in Table 6.2. In order to achieve more realistic analysis, we used real input values

(such as the construction cost, typical maintenance cost/frequency, and work hours/duration) provided by NDOR. Four alternatives were evaluated in this study: LCCA of pavement structures with the thin lift SLX (one-inch milling-overlay) and SPH (two-inch milling-overlay) at low and high volume traffic conditions for a total 30-year analysis period. With the given traffic conditions, the service life of each alternative was estimated by the agency based on the past practice experience (for SPH) and expected performance life (for SLX), as presented in Table 6.2. Since each project is differentiated by only the rehabilitation practice (SLX vs. SPH) and its expected service life, for the sake of simplicity, the history (or activities) of the existing pavement structure was not considered in the LCCA estimation.

Table 6.2 Summary of cost inputs for each alternative and detail traffic inputs

Alternative 1: SPH overlay at high volume traffic (10 year service life)					
Activity	No. of activities	Construction Cost (\$/1-mi length)	Maintenance Frequency (yrs)	Maintenance cost (\$/1-mi length)	Work duration (days)
2" Mill & 2" SPH Overlay	3 ^a	190,000*	5*	15,000*	0.3*
Alternative 2: SLX overlay at high volume traffic (6 year service life)					
1" Mill & 1" SLX Overlay	5 ^a	95,000*	5*	15,000*	0.15*
Alternative 3: SPH overlay at low volume traffic (15 year service life)					
2" Mill & 2" SPH Overlay	2 ^a	190,000*	7.5*	15,000*	0.3*
Alternative 4: SLX overlay at Low volume traffic (10 year service life)					
1" Mill & 1" SLX Overlay	3 ^a	95,000*	5*	15,000*	0.15*
Traffic inputs					
Parameters			High volume traffic	Low volume traffic	
AADT Construction Year (total for both directions)			18,098*	2,884*	
Total Trucks as Percentage of AADT (%)			39*	14*	
Annual Growth Rate of Traffic (%)			2.0*	2.0*	
Speed Limit Under Normal Operating Conditions (mph)			75*	60*	
Work Zone Speed Limit (mph)			55*	45*	
Discount Rate (%)			2.0 ^a		
Value of Time for Passenger Cars (\$/hour)			13.96 ^d		
Value of Time for Single Unit Trucks (\$/hour)			22.34 ^d		
Value of Time for Combination Trucks (\$/hour)			26.89 ^d		

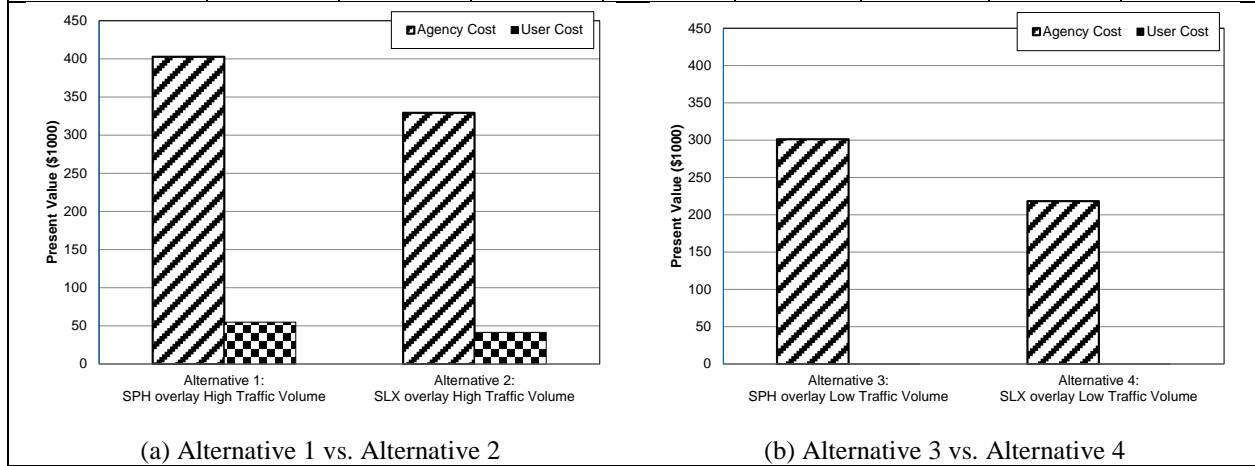
^aTypical, ^dDefault inputs, and *Inputs provided by NDOR

Table 6.3 presents the LCCA results. Both the agency costs and user costs of each alternative are summarized in terms of net present value and equivalent uniform annual cost (EUAC). As shown in the table, the SLX-overlay pavement resulted in lower agency and user costs at both high and low traffic conditions than the SPH-overlay practices. The analysis results clearly support the benefits of the thin-lift asphalt overlay practice, e.g., 1) reduced initial costs, 2) minimized traffic delays, and 3) the ability to handle heavy traffic, and 4) improving IRI more

frequently in shorter intervals through the service life of the overlays. Public perception and the impact to the road user are greatly improved when production of thin lift overlays is expedited, at an average of paving 3 lane miles per day. For example, a typical 8 to 10 mile – roadway segment only requires approximately one week to construct. Through shorter project construction windows, the agency can deliver new/smooth surfacing extremely fast, and can easily be constructed during night and weekend paving to accommodate traffic issues for heavy volume corridors. The thin lift SLX mix design is also very cost effective by utilizing RAP contents of 30-35% and taking full advantage of roadway millings that are processed through either crushing or screening to insure the RAP is sized to accommodate the 1 inch lift thickness. Not only can it be used in standard overlays and thin lift overlays for pavement preservation, it can also be used in conjunction with full depth repair projects to aid in maintaining a roadways service life until a roadway or urban section can be replaced.

Table 6.3 Summary of the LCCA analysis results

Total Cost	Alternative 1: SPH overlay high traffic volume		Alternative 2: SLX overlay high traffic volume		Alternative 3: SPH overlay low traffic volume		Alternative 4: SLX overlay low traffic volume	
	Agency Cost (\$1000)	User Cost (\$1000)	Agency Cost (\$1000)	User Cost (\$1000)	Agency Cost (\$1000)	User Cost (\$1000)	Agency Cost (\$1000)	User Cost (\$1000)
<i>Undiscounted Sum</i>	\$425.00	\$56.60	\$360.00	\$43.10	\$315.00	\$0.13	\$235.00	\$0.09
Present Value	\$402.71	\$54.79	\$329.27	\$41.47	\$301.23	\$0.12	\$218.29	\$0.08
EUAC	\$17.98	\$2.45	\$14.70	\$1.85	\$13.45	\$0.01	\$9.75	\$0.00



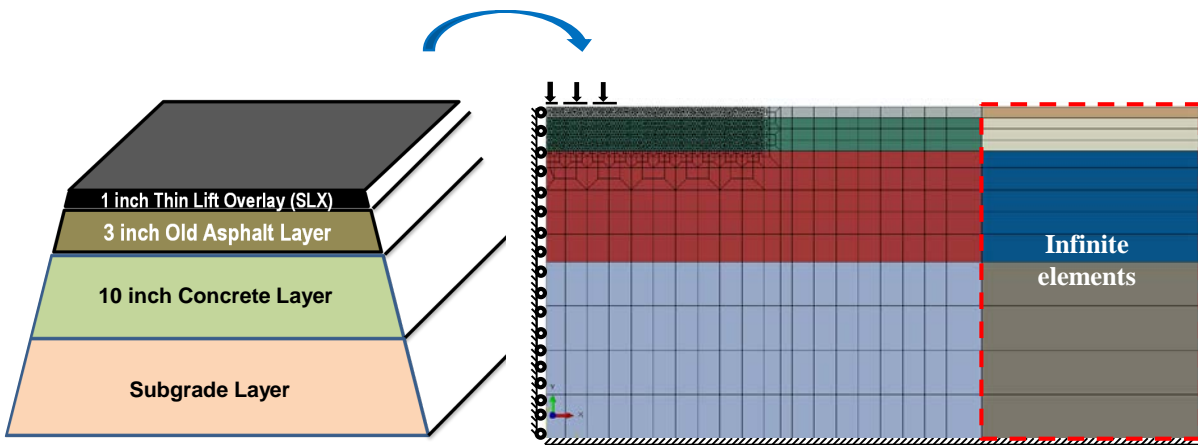
6.3 Finite Element Modeling

Two-dimensional finite element modeling was conducted to investigate mechanical behaviors of the two different pavement structures. The developed viscoelastic, viscoplastic, and viscodamage constitutive law was implemented in a commercial package, Abaqus Version 6.10 (Abaqus 2010) via user material subroutine, UMAT. Permanent deformation (i.e., rutting) was predicted at a high temperature (i.e., 40 °C) by considering asphalt overlays as a viscoelastic-viscoplastic material, while the viscoelastic-viscodamage response of asphalt overlays was considered in fatigue cracking simulations at an intermediate temperature (i.e., 21 °C).

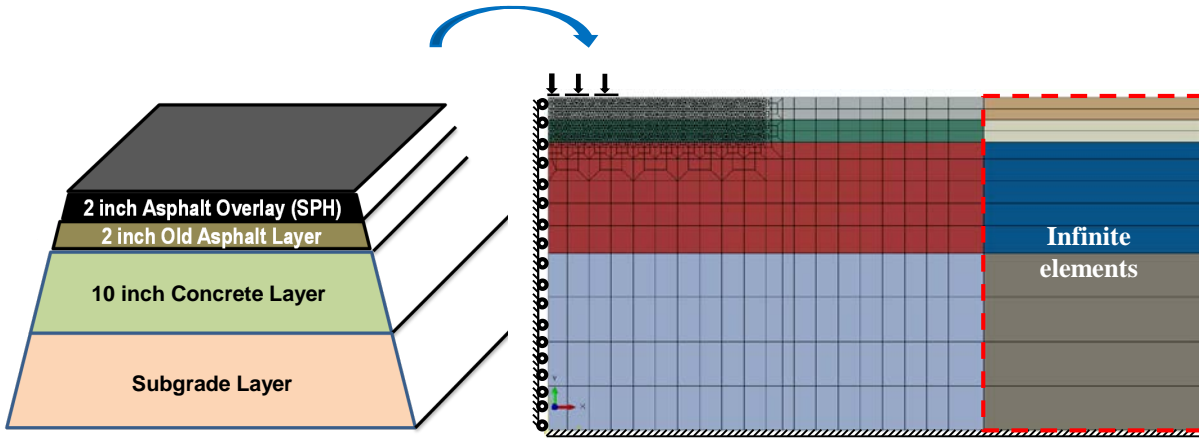
6.3.1 Pavement model geometry and boundary conditions

Pavement structures with the two different asphalt overlays (SLX vs. SPH) were modeled for performance predictions, as shown in Figure 6.4. An SLX overlay with 25.4 mm thickness,

old asphalt layer with 76.2 mm thickness, concrete layer with 254.0 mm thickness, and subgrade layers with 406.4mm thickness were included in the SLX pavement model, while different thicknesses for SPH overlay (50.8 mm) and the old asphalt layer (50.8 mm) were used for the SPH pavement. The left side of the model had a symmetric boundary condition and the bottom of the model was fixed. As illustrated in Figure 6.4, infinite elements were employed to minimize the effect from surrounding media on simulation results. Additionally, transitional meshing techniques were adopted to reduce computational time. Half of a single tire in a dual tire, as shown in Figure 6.5 (a), was considered. Based on a study by Yoo et al. (2006), three different vertical pressures at each tire rib were applied to the left-top of the pavement models, as shown in Figure 6.5 (b). The width of the tire ribs and the corresponding vertical pressures are summarized in Table 6.4.

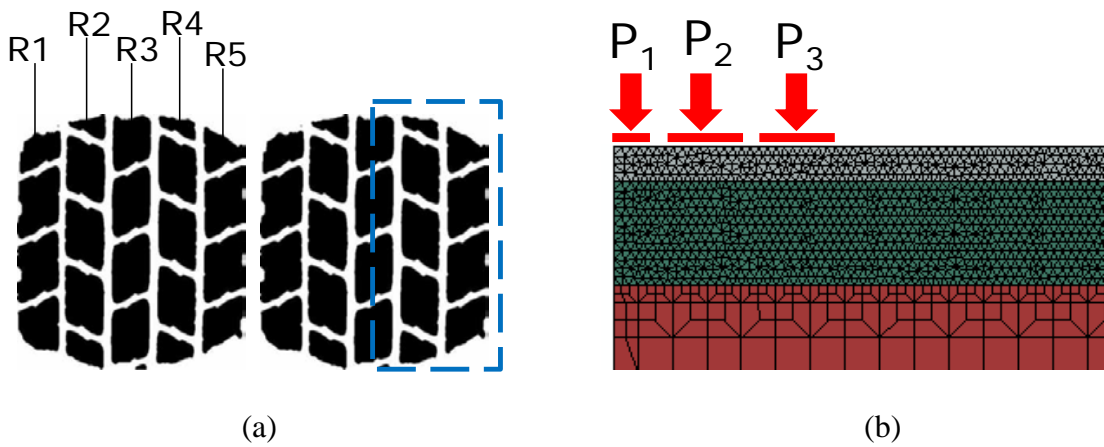


(a) SLX pavement structure



(b) SPH pavement structure

Figure 6.4 Geometry and boundary condition for two pavement structures



(a)

(b)

Figure 6.5 (a) Dual tire foot print (Yoo et al. 2006) and (b) three vertical pressures applied on the pavement structures

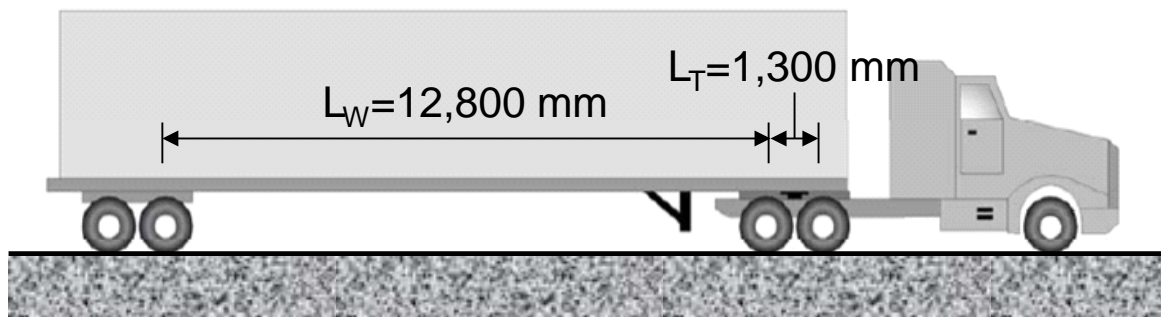
Table 6.4 Dual tire configuration for each rib (Yoo et al. 2006)

	Width (mm)	Vertical pressure (kPa)
R1, R5	34.0	640=P1
R2, R4	30.0	860=P2
R3	32.5	990=P3

Based on the Class 9 truck (see Figure 6.6 (a)) used in this study, the loading configuration was calculated by:

$$\begin{aligned} \text{Loading time} &= \frac{L_T}{v} \\ \text{Resting time} &= \frac{L_W}{v} \end{aligned} \tag{6-1}$$

where L_T is the width between each tire at one axle, L_W is the length between each axle, and v is the vehicle speed. In this study, a 60 mile/h (96.6 km/h) vehicle speed was used. The calculated loading configuration is shown in Figure 6.6 (b), where loading and resting times are 0.05 s and 0.6 s, respectively. It is noted that one cycle for a tandem-axle truck was composed of two loading times and one resting time. In this study, it was assumed that there was no resting time between passing trucks.



(a)

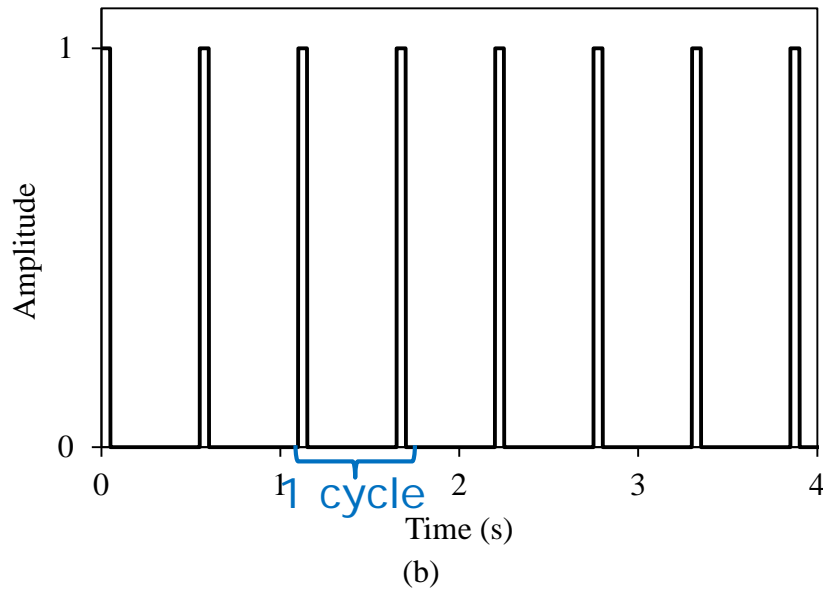


Figure 6.6 (a) Class 9 truck configuration (Soares et al. 2008) and (b) loading configuration for a vehicle speed of 60 mile/h

6.3.2 Layer properties

Material properties of the individual layers for the simulation are summarized in Table 6.5. Viscoelastic, viscoplastic, and viscodamage parameters for asphalt overlays and the old asphalt layer were converted for a reference temperature of 21 °C, while viscoplastic parameters were obtained from the static creep-recovery tests with various stress levels at 30 °C. The asphalt overlays were considered as a viscoelastic-viscoplastic material for rutting simulations and a viscoelastic-viscodamage material for the fatigue cracking simulation. For the old asphalt layer, only viscoelastic material properties of SP5 obtained from the MEPDG simulation were used. The underlying layers such as concrete and subgrade layers were modeled as an isotropic linear elastic material, as presented in the table.

Table 6.5 Material properties of each layer

Asphalt overlay									
SPH					SLX				
Viscoelastic material properties ($T_{ref} = 21^{\circ}\text{C}$)									
n	$\lambda_n(\text{s}^{-1})$	$D_n(\text{MPa}^{-1})$			n	$\lambda_n(\text{s}^{-1})$	$D_n(\text{MPa}^{-1})$		
0	-	6.69×10^{-5}			0	-	7.24×10^{-5}		
1	1.41×10^4	2.85×10^{-5}			1	1.04×10^4	3.08×10^{-5}		
2	1.84×10^3	3.24×10^{-5}			2	1.37×10^3	3.34×10^{-5}		
3	2.40×10^2	6.31×10^{-5}			3	1.80×10^2	7.04×10^{-5}		
4	3.13×10^1	1.30×10^{-4}			4	2.37×10^1	1.46×10^{-4}		
5	4.08×10^0	2.52×10^{-4}			5	3.12×10^0	2.95×10^{-4}		
6	5.32×10^{-1}	5.21×10^{-4}			6	4.10×10^{-1}	6.20×10^{-4}		
7	6.94×10^{-2}	1.76×10^{-3}			7	5.39×10^{-2}	2.11×10^{-3}		
8	9.05×10^{-3}	3.30×10^{-3}			8	7.09×10^{-3}	3.90×10^{-3}		
9	1.18×10^{-3}	8.11×10^{-3}			9	9.33×10^{-4}	9.17×10^{-3}		
Viscoplastic material properties ($T_{ref} = 21^{\circ}\text{C}$)									
Γ_0^{vp} (1/s)	N	k_0 (kPa)	k_1 (kPa)	k_2	Γ_0^{vp} (1/s)	N	k_0 (kPa)	k_1 (kPa)	k_2
4.15×10^{-5}	1.23	90.71	1945.15	142.54	5.80×10^{-5}	1.40	98.84	1903.85	126.52
Viscodamage material properties ($T_{ref} = 21^{\circ}\text{C}$)									
Γ_0^{vd} (1/s)	q	k	Y_0 (kPa)	Γ_0^{vd} (1/s)	q	k	Y_0 (kPa)		
8.55×10^{-17}	4.85	-2.40	1000	2.86×10^{-18}	5.51	-2.45	1000		
Old asphalt layer (SP5) ($T_{ref} = 21^{\circ}\text{C}$)									
n	$\lambda_n(\text{s}^{-1})$			$D_n(\text{MPa}^{-1})$					
0	-			4.23×10^{-5}					
1	2.00×10^3			1.76×10^{-5}					
2	2.00×10^2			2.11×10^{-5}					
3	2.00×10^1			3.98×10^{-5}					
4	2.00×10^0			8.02×10^{-5}					
5	2.00×10^1			1.59×10^{-4}					
6	2.00×10^{-2}			3.66×10^{-4}					
7	2.00×10^{-3}			5.36×10^{-4}					
8	2.00×10^{-4}			2.23×10^{-3}					
9	4.00×10^{-5}			8.06×10^{-4}					
Concrete layer									
E(MPa)					v				
2.66×10^4					0.20				
Subgrade layer									
E(MPa)					v				
1.00×10^2					0.35				

6.3.3 *Simulation results*

In this subsection, simulation results are presented to compare the structural performance of the two pavements with SLX and SPH in terms of permanent deformation and fatigue cracking. Permanent deformation (rutting) simulations were conducted at 40 °C until 3,000 cycles, where asphalt overlays (i.e., SLX and SPH) were considered as a viscoelastic-viscoplastic material. The material parameters for a reference temperature (21°C) in Table 6.5 were converted for simulation temperature (i.e., 40 °C) by using the time-temperature shift factors. Rutting was measured from a node at left-top of the pavement models, as shown in Figure 6.7. Since there was no information on the current status of the SP5 old asphalt layer, the viscoelastic property obtained from a previous study (Im et al. 2010) was varied with 50%, 100%, and 150% of its virgin state. This enabled investigation of the effect of old asphalt layer, which could be stiffer due to aging or deteriorated due to damage, on the pavement permanent deformation.

Figure 6.8 presents the comparison of rutting between SLX and SPH pavement structures for each case, indicating that about 15% more rutting occurred in the SPH pavement structure compared to rutting developed in the SLX pavement structure. However, overall rutting from the two structures after 3,000 truck cycles was not significant (less than 0.40 mm) comparing to the typical failure limit (9 mm in Nebraska (NDOR 2013)). It was also observed that more rutting was accumulated when 50% stiffness of SP5 layer from its virgin state was used as the property of the old asphalt layer due to more rutting potential from the deteriorated old layer. Figure 6.9 through Figure 6.11 show contour plots of vertical displacement distributions in the asphalt overlay and old asphalt layer for different loading cycles obtained from the two pavement structures. Although contour maps of the two pavement structures seem different, variation in the vertical displacements between the two structures is small because the gap between the vertical

displacements for each contour color is 0.025 mm. This implies that the SLX pavement rutting will be similar to or slightly less than the SPH pavement structure, which needs further validation with field performance monitoring.

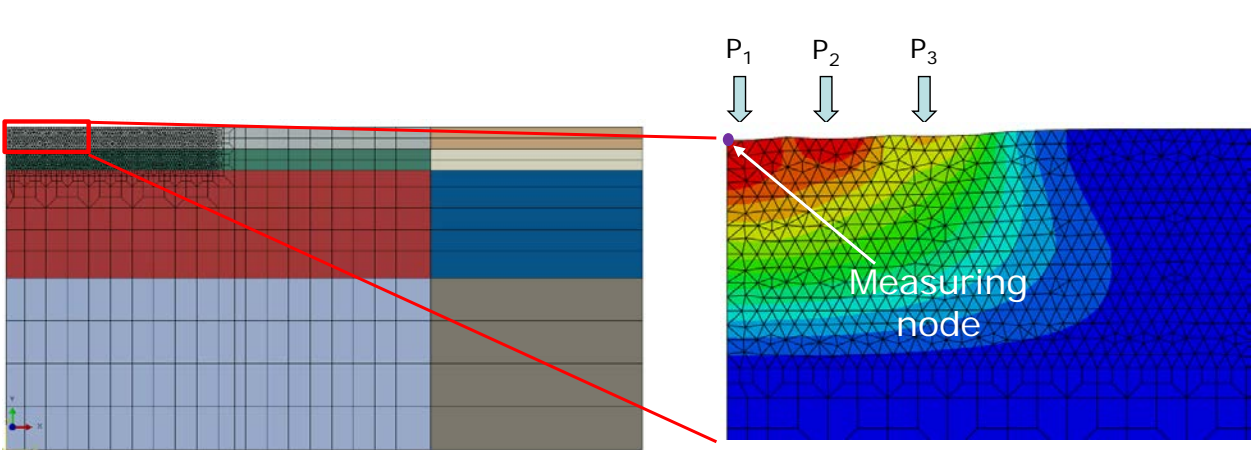
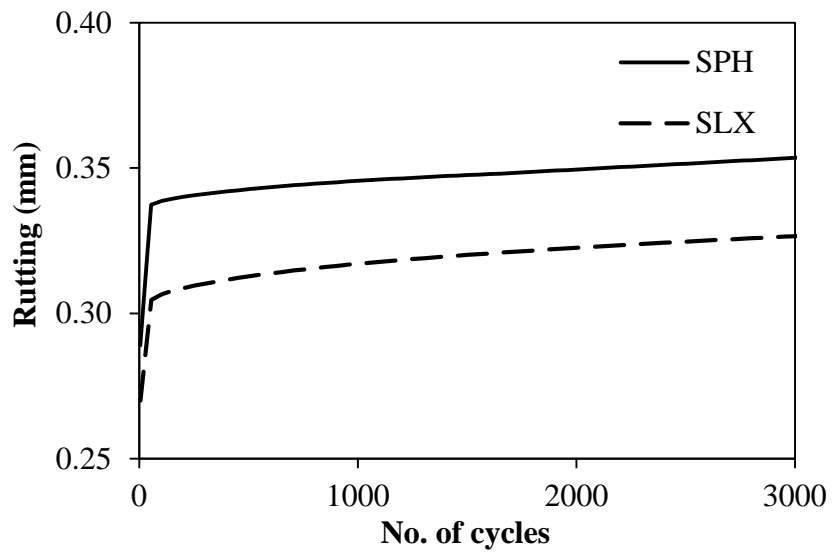
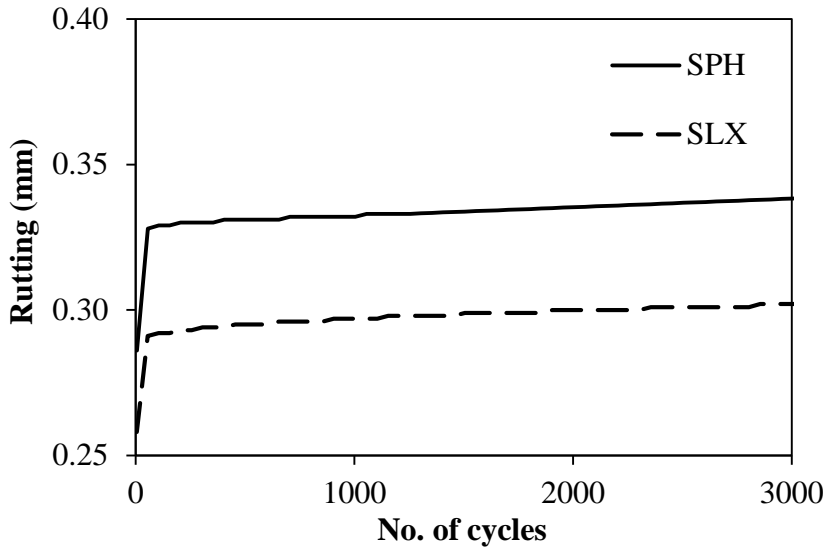


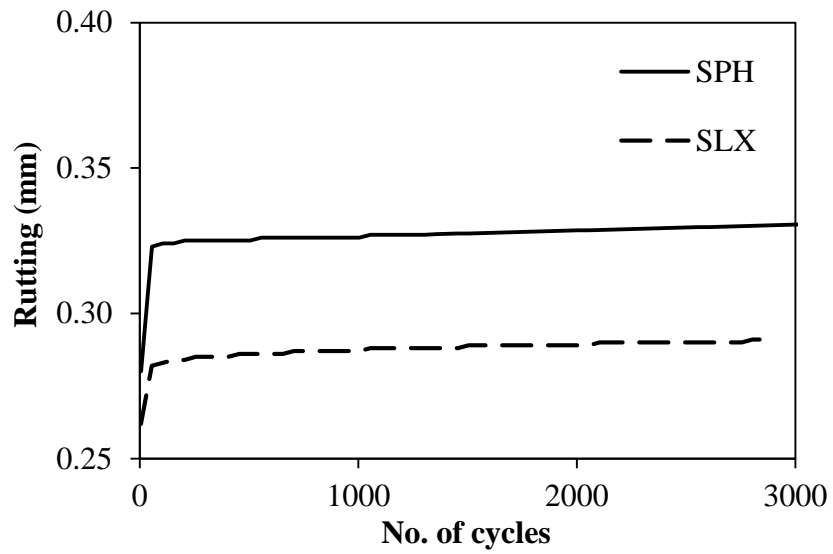
Figure 6.7 Node where rutting was measured in the pavement model



(a) 50% of SP5



(b) 100% of SP5



(c) 150% of SP5

Figure 6.8 Comparison of rutting between SLX and SPH pavement structures with different old asphalt layer properties

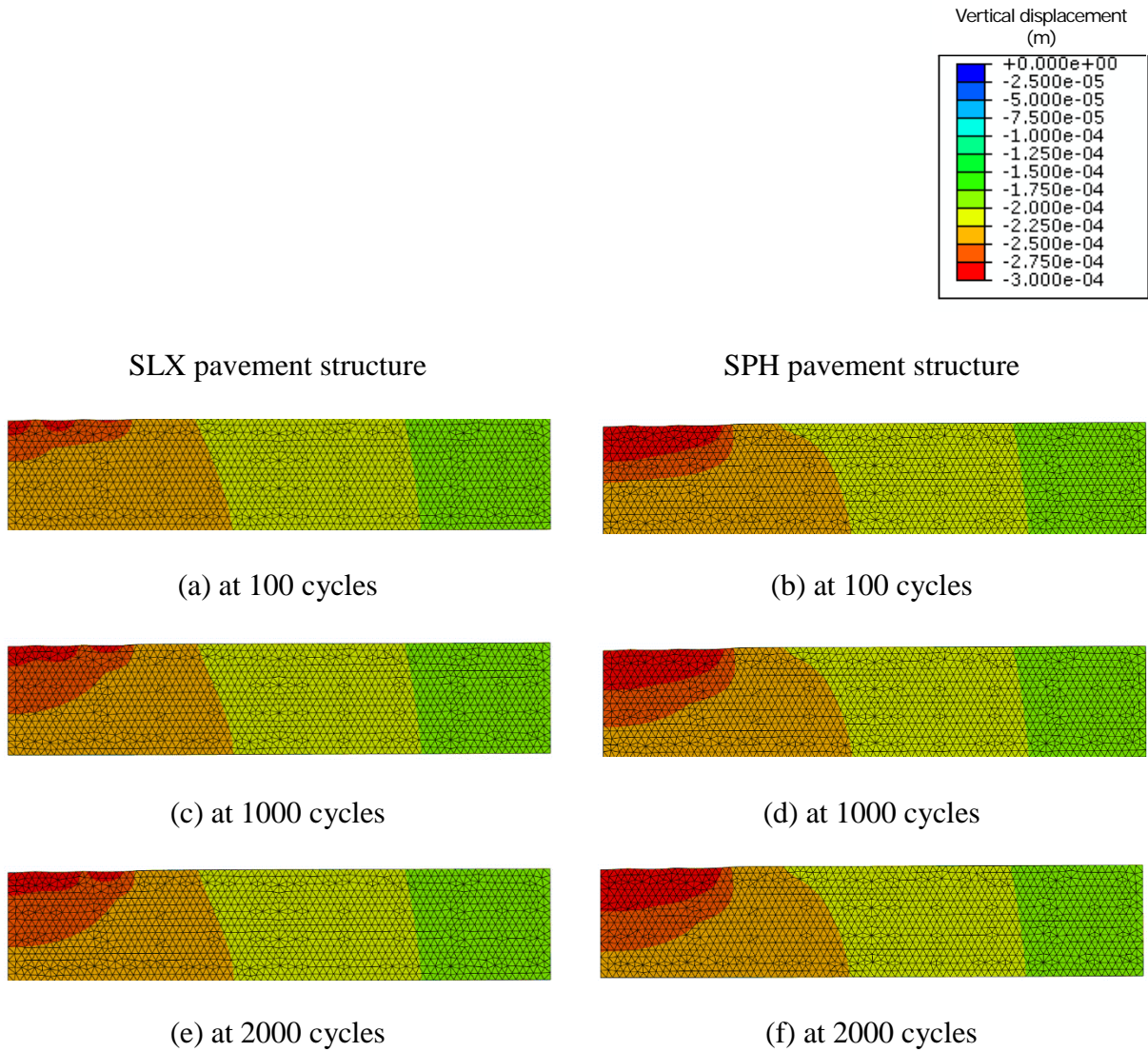


Figure 6.9 Vertical displacement distribution contours of SLX and SPH pavement structures when 50% of SP5 viscoelastic property was used for old asphalt layer

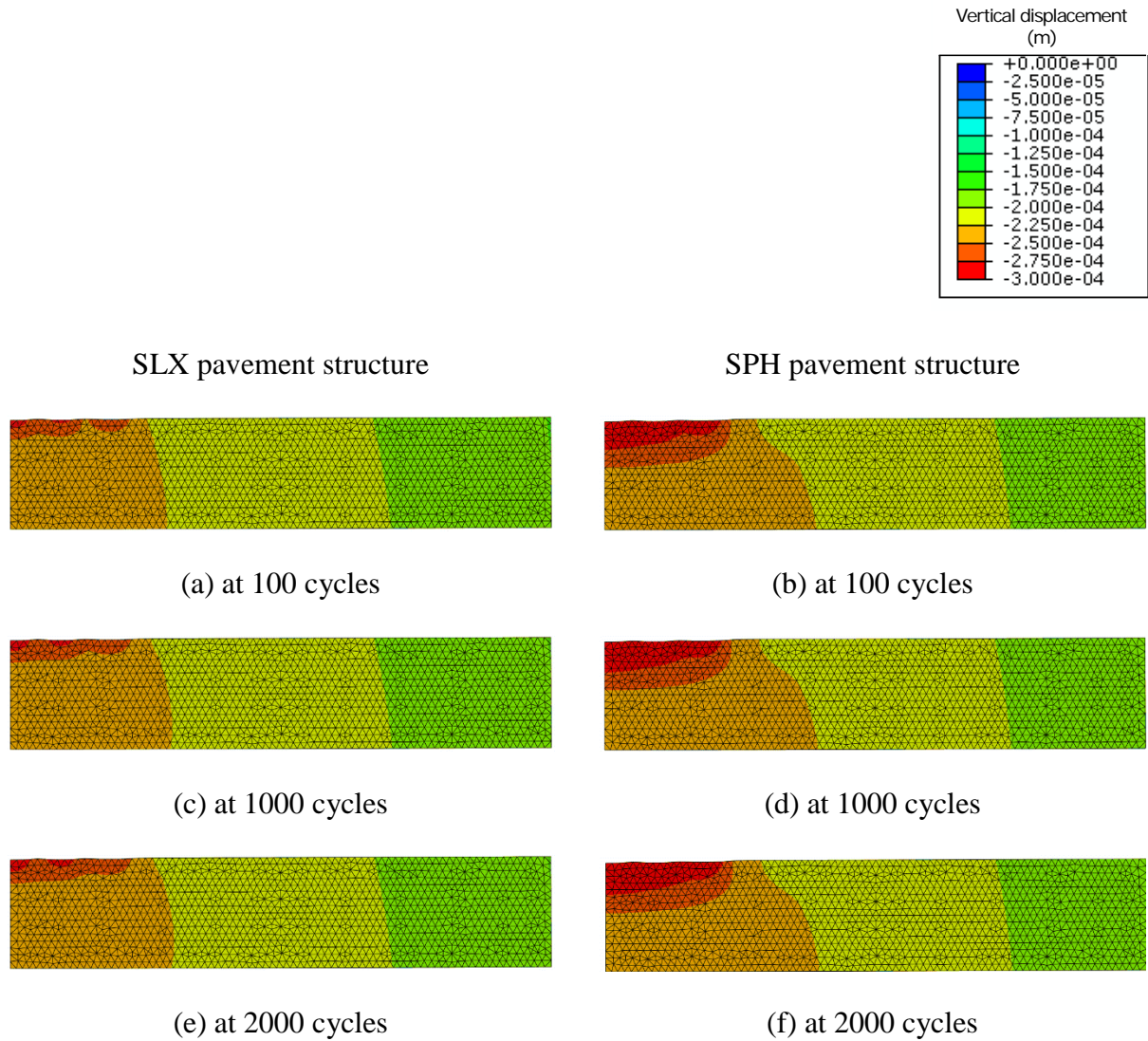


Figure 6.10 Vertical displacement distribution contours of SLX and SPH pavement structures when 100% of SP5 viscoelastic property was used for old asphalt layer

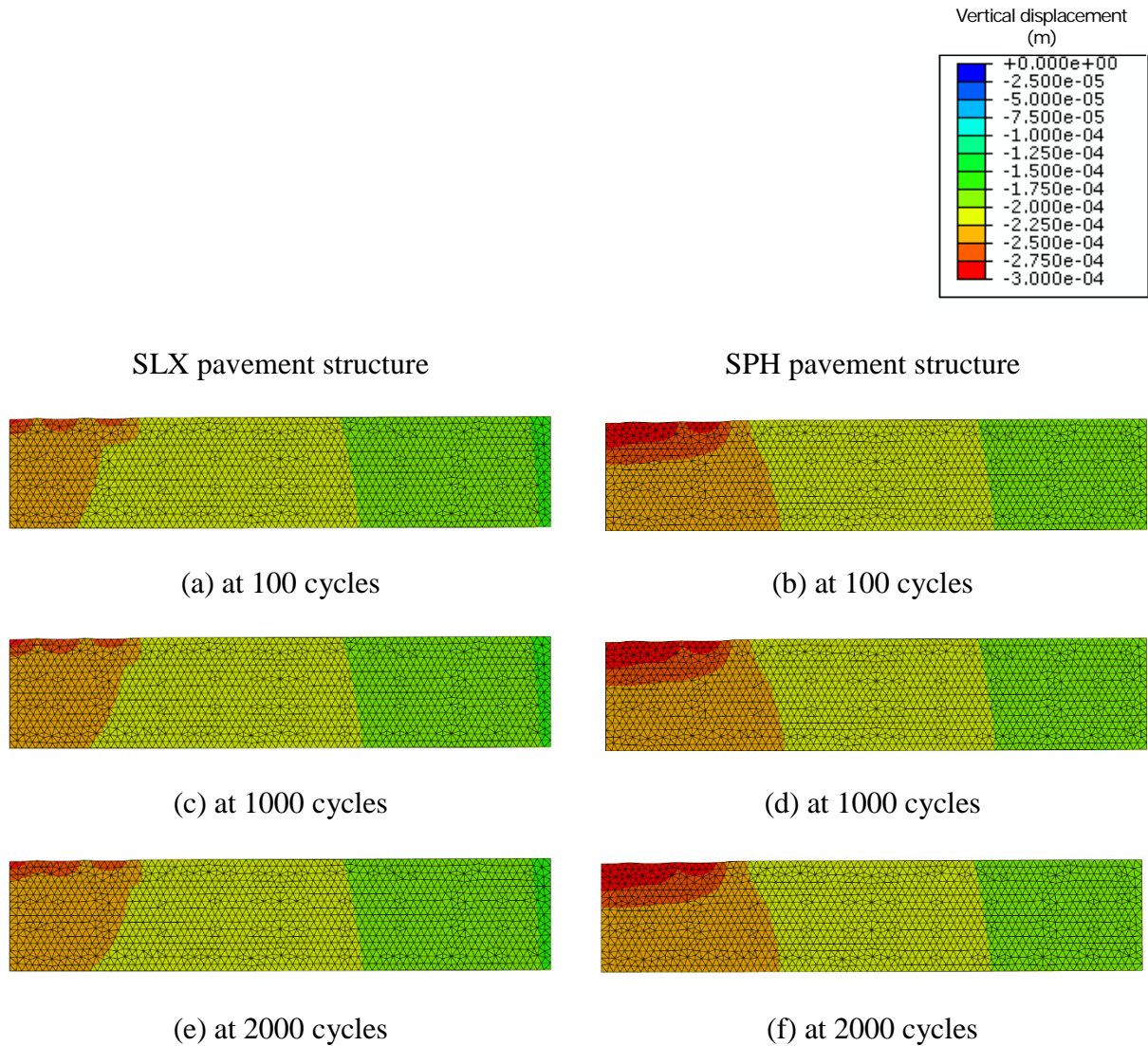


Figure 6.11 Vertical displacement distribution contours of SLX and SPH pavement structures when 150% of SP5 viscoelastic property was used for old asphalt layer

To conduct fatigue cracking simulation, the two different asphalt overlays were considered viscoelastic-viscodamage materials subjected to 3,000 truck loading cycles at 21 °C. For the old asphalt layer property, 150% viscoelastic stiffness of SP5 from its virgin state was used because cracking is more critical on a stiffer layer. Figure 6.12 shows damage density contours of the two pavement structures. Contour maps show that the SLX pavement structure is

less fatigue damage susceptible than the SPH pavement structure, although the damage density values are extremely small. Damage density (ϕ) has a range from 0 to 1, where $\phi = 0$ means that the material is intact, while $\phi = 1$ means that the material is fully damaged. It clearly implies that the SLX pavement cracking will not at least be more than the SPH pavement structure, which also needs further validation with field performance monitoring.

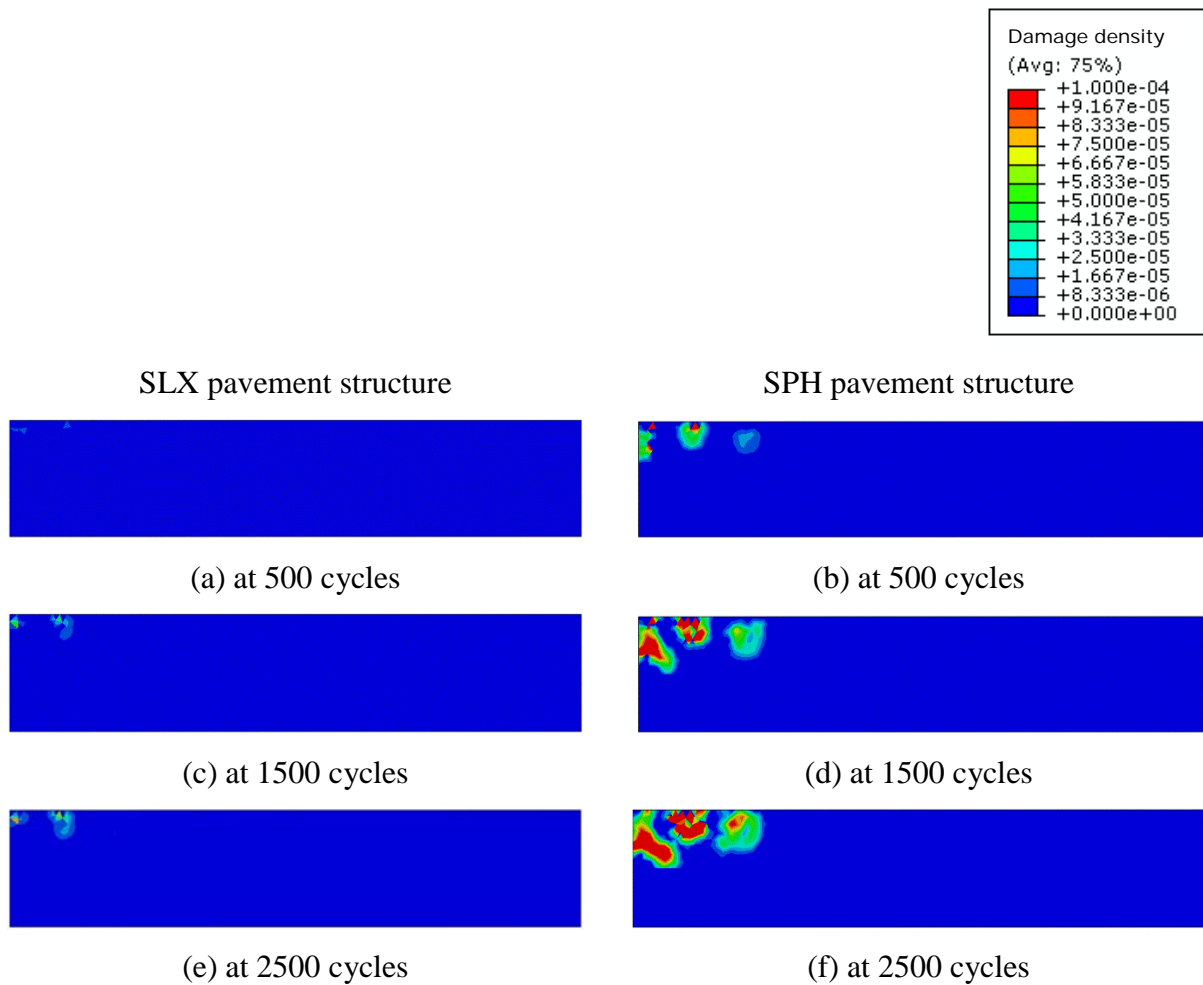


Figure 6.12 Damage density distribution contours of SLX and SPH pavement structures when 150% of SP5 viscoelastic property was used for old asphalt layer

Chapter 7 Summary and Conclusions

Thin asphalt overlays have been widely used because of many benefits, such as long service life, low life cycle cost, improved ride quality, etc., but the thin lift overlay application is a relatively new preservation and treatment application. Although the experience with this technique has been demonstrated as positive, potential problems and unknowns still exist. In this study, thin lift overlay with a SLX mixture, newly implemented in Nebraska, and the current Nebraska overlay with a SPH mixture were evaluated. One-inch (25.4 mm) thick SLX mixture and two-inch (50.8 mm) thick SPH mixture were overlaid on top of milled old asphalt layers on I-80 Exit 279 near Kearney, Nebraska. A series of laboratory tests, such as the dynamic modulus, dynamic creep, static multiple stress creep-recovery, Hamburg wheel tracking, and semi-circular bending fracture tests were conducted to characterize the mechanical properties and performance characteristics of each mixture. These laboratory tests were then used to identify material properties in order to conduct pavement performance predictions with two different approaches: the MEPDG simulation and the finite element model simulation. In addition, an LCCA was performed to investigate the economic benefits of the thin-lift overlay compared to the conventional overlay practice.

The following bullet points summarize the conclusions that can be drawn:

- The viscoelastic stiffness properties of the SLX and SPH mixtures were characterized by dynamic modulus tests at various temperatures and loading frequencies. Test results presented similar stiffness characteristics between the two mixtures.
- Dynamic creep tests were conducted to evaluate the rutting resistance, where there were no significant differences between the two mixtures.

- The semi-circular bending test results and their further incorporation into the cohesive zone fracture law indicated that the cracking resistance of the SLX mixture is similar to or slightly better than that of the SPH mixture.
- The moisture susceptibility of the mixtures were measured by the Hamburg wheel tracking test. Although the test results showed that the SLX mixture was more susceptible to moisture-induced damage, it needs further investigation through field performance monitoring, since the Hamburg test is somewhat limited in representing actual field performance related to the moisture damage of mixtures.
- MEPDG simulation predicted that both pavements will perform satisfactorily during the expected design life, while it is expected from the LCCA that the thin SLX preservation practice can reduce both the agency costs and the users costs compared to the conventional SPH rehabilitation practice.
- Pavement performance simulation results from the finite element analysis showed that the thin-lift overlay practice with the SLX mixtures would not compromise pavement resistance to rutting and cracking compared to the conventional rehabilitation practices.
- Both performance prediction results need to be compared to actual field performance data. To date, one-year field performance is available and field performance monitoring will be continued.

References

- AASHTO (2008). "AASHTO TP 62-07 Determining the Dynamic Modulus of Hot Mix Asphalt (HMA) Concrete Mixture." American Association of State and Highway Transportation Officials, Washington, D.C.
- AASHTO (2011). "AASHTO T 324-11 Hamburg Wheel-Track Testing of Compacted Hot Mix Asphalt (HMA)." American Association of State and Highway Transportation Officials, Washington, D.C.
- AASHTO (2011). "AASHTO TP 79-11 Determining the Dynamic Modulus and Flow Number for Hot Mix Asphalt (HMA) Using the Asphalt Mixture Performance Tester (AMPT)." American Association of State and Highway Transportation Officials, Washington, D.C.
- Abaqus (2010). *User's Manual Version 6.10*, Habbit, Karlsson and Sorensen, Inc., Providence, RI.
- Ahmed, S., Dave, E. V., Buttlar, W. G., and Exline, M. K. (2013). "Cracking resistance of thin-bonded overlays using fracture test, numerical simulations and early field performance." *International Journal of Pavement Engineering*, 14(6), 540-552.
- Baek, J., and Al-Qadi, I. (2009). "Reflective cracking: Modeling fracture behavior of hot-mix asphalt overlays with interlayer systems." *Asphalt Paving Technology-Proceedings*, 28, 789-824.
- Ban, H., Im, S., and Kim, Y.-R. (2013). "Nonlinear viscoelastic approach to model damage-associated performance behavior of asphaltic mixture and pavement structure." *Canadian Journal of Civil Engineering*, 40(4), 313-323.
- Bazant, Z. P., and Planas, J. (1997). *Fracture and size effect in concrete and other quasibrittle materials*, CRC press, Boca Raton, FL.
- Brown, E. R., and Heitzman, M. (2013). "THIN HMA OVERLAYS FOR PAVEMENT PRESERVATION AND LOW VOLUME ASPHALT ROADS." National Center for Asphalt Technology, NCAT Report 13-05, Auburn, AL.
- Darabi, M. K., Al-Rub, R. K. A., Masad, E. A., and Little, D. N. (2013). "Constitutive modeling of fatigue damage response of asphalt concrete materials with consideration of micro-damage healing." *International Journal of Solids and Structures*, 50(19), 2901-2913.
- Dave, E. V., and Buttlar, W. G. (2010). "Thermal reflective cracking of asphalt concrete overlays." *International Journal of Pavement Engineering*, 11(6), 477-488.
- Druta, C., Wang, L., and McGhee, K. K. (2014). "Performance Evaluation of Thin Wearing Courses Through Scaled Accelerated Trafficking." FHWA/VCTIR 14-R7, Virginia Center for Transportation Innovation and Research, Richmond, VA.

- Duan, K., Hu, X., and Wittmann, F. H. (2006). "Scaling of quasi-brittle fracture: Boundary and size effect." *Mechanics of Materials*, 38(1), 128-141.
- Espinosa, H. D., and Zavattieri, P. D. (2003). "A grain level model for the study of failure initiation and evolution in polycrystalline brittle materials. Part I: Theory and numerical implementation." *Mechanics of Materials*, 35(3), 333-364.
- FHWA (2006). "Pavement Preservation Compendium II." National Center for Pavement Preservation Foundation for Pavement Preservation (FHWA).
- FHWA (2010). "Life-Cycle Cost Analysis - RealCost Use Manual" National Center for Pavement Preservation Foundation for Pavement Preservation (FHWA).
- Geubelle, P. H., and Baylor, J. S. (1998). "Impact-induced delamination of composites: a 2D simulation." *Composites Part B: Engineering*, 29(5), 589-602.
- Gibson, N., Shenoy, A., Al-Khateeb, G., Kutay, M., Youtchef, J., and Harman, T. (2010). "Full-scale accelerated performance testing for superpave and structural validation." *Final Report FHWA-RD-xx-xxxx*, Federal Highway Administration.
- Guthrie, W. S., and Butler, M. J. "Field Evaluation of Asphalt Overlays on State Route 30 in Northern Utah." *Proc., Transportation Research Board 90th Annual Meeting*.
- Hoerner, T. E., Zimmerman, K. A., Smith, K. D., and Cooley, L. A. (2007). "Mechanistic-Empirical Pavement Design Guide Implementation Plan." *Study SD2005-01 Final Report*, South Dakota Department of Transportation.
- Im, S., Kim, Y.-R., and Ban, H. (2010). "Layer Moduli of Nebraska Pavements for the New Mechanistic-Empirical Pavement Design Guide (MEPDG)." Report No. MPM-08, University of Nebraska-Lincoln, Department of Civil Engineering, Lincoln, NE.
- Im, S., You, T., Ban, H., and Kim, Y. -R.(2015). "Multiscale testing-analysis of asphaltic materials considering viscoelastic and viscoplastic deformation" *INTERNATIONAL JOURNAL OF PAVEMENT ENGINEERING*
(<http://dx.doi.org/10.1080/10298436.2015.1066002>)
- Jahren, C., Smith, D. E., and Plymesser, C. (2007). "Thin Maintenance Surfaces Handbook." Center for Transportation Research and Education, Iowa State University.
- Johanneck, L., Clyne, T., Tompkins, D., and Khazanovich, L. "Evaluation and Local Calibration of MEPDG EICM Model Using MnRoad Data." *Proc., 90th Annual Meeting of the Transportation Research Board, Washington, DC*, Transportation Research Board.
- Khazanovich, L., Tompkins, D., Wu, R., and Harvey, J. (2013). "Investigation and Modification of Available Mechanistic-Empirical Procedures for Reflective Cracking in Asphalt

- Overlays of Concrete Pavements." *Transportation Research Record: Journal of the Transportation Research Board* (2368), 126-132.
- Kim, H., Wagoner, M. P., and Buttlar, W. G. (2008). "Simulation of fracture behavior in asphalt concrete using a heterogeneous cohesive zone discrete element model." *Journal of Materials in Civil Engineering*, 20(8), 552-563.
- Lai, J., and Bakker, A. (1996). "3-D Schapery representation for non-linear viscoelasticity and finite element implementation." *Computational Mechanics*, 18(3), 182-191.
- Lemaitre, J., and Chaboche, J. (1990). "Mechanics of solid materials." Cambridge University Press, Cambridge, UK.
- Marasteanu, M., Zofka, A., Turos, M., Li, X., Velasquez, R., Li, X., Buttlar, W., Paulino, G., Braham, A., and Dave, E. (2007). "Investigation of low temperature cracking in asphalt pavements national pooled fund study 776." *Final Report No. MN/RC 2007-43*, Minnesota Department of Transportation, Saint Paul, MN.
- Masad, E., Dessouky, S., and Little, D. (2007). "Development of an elastoviscoplastic microstructural-based continuum model to predict permanent deformation in hot mix asphalt." *International Journal of Geomechanics*, 7(2), 119-130.
- Masad, E., Tashman, L., Little, D., and Zbib, H. (2005). "Viscoplastic modeling of asphalt mixes with the effects of anisotropy, damage and aggregate characteristics." *Mechanics of Materials*, 37(12), 1242-1256.
- MDOT (2005). "Guide Specification for HMA Ultra-Thin." Michigan Department of Transportation.
- Mogawer, W., S, Austerman, A. J., Kluttz, R. Q., and Mohammad, L. N. (2013). "Development, Implementation, and Verification of Performance Based Specifications for High Performance Thin Lift Overlay Mixtures." *Transportation Research Board 92nd Annual Meeting* (13-2728).
- NDOR (2013). "2013 NDOR Pavement Design Manual." M. a. R. Division, ed., Nebraska Department of Roads, Lincoln, NE.
- Newcomb, D. E. (2009). "Thin asphalt overlays for pavement preservation." National Asphalt Pavement Association, Lanham, MD.
- Nicholls, J. C., Carswell, I., and Langdale, P. (2002). "Durability of Thin Asphalt Surfacing Systems: Part 1 Initial Findings." *TRL REPORT 557*.
- Norouzi, M., Nassiri, S., Haghi, N. T., and Bayat, A. (2014). "Performance Evaluation of Asphalt overlays in Alberta using Long Term Pavement Performance Specific Pavement Study 5 Sections." *International Journal of Pavement Research and Technology*, 7(1), 60.

- NYDOT (2008). "REVISED SPECIAL SPECIFICATIONS FOR 6.3-mm POLYMER-MODIFIED HOT MIX ASPHALT (HMA)." New York Department of Transportation.
- ODOT (2002). "Technical Bulletin: Smoothseal (ODOT, SS 854, Fine Graded Polymer Asphalt Concrete), Overlays for Use as Preventive Maintenance Surface Treatments." Ohio Department of Transportation.
- Park, S., and Schapery, R. (1999). "Methods of interconversion between linear viscoelastic material functions. Part I—A numerical method based on Prony series." *International Journal of Solids and Structures*, 36(11), 1653-1675.
- Perzyna, P. (1971). "Thermodynamic theory of viscoplasticity." *Advances in Applied Mechanics*, 11, 313-354.
- Powell, R. B., and Buchanan, S. (2012). "Long term performance of a thin asphalt overlay on the NCAT pavement test track." *Transportation Research Board (TRB) 91st Annual Meeting Compendium of Papers DVD*.
- Pretorius, F., Wise, J., and Henderson, M. (2004). "Development of application differentiated ultra-thin asphalt friction courses for southern African application." *Proceedings of the 8th Conference on Asphalt Pavements for Southern Africa (CAPSA'04)*, 12, 16.
- Schapery, R. A. (1969). "On the characterization of nonlinear viscoelastic materials." *Polymer Engineering & Science*, 9(4), 295-310.
- Scullion, T., Zhou, F., Walubita, L., and Sebesta, S. (2009). "DESIGN AND PERFORMANCE EVALUATION OF VERY THIN OVERLAYS IN TEXAS." FHWA/TX-09/0-5598-2, Texas Transportation Institute, Texas A&M University, College Station, Texas.
- Seibi, A. C., Sharma, M. G., Ali, G. A., and Kenis, W. J. (2001). "Constitutive relations for asphalt concrete under high rates of loading." *Transportation Research Record: Journal of the Transportation Research Board*, 1767, 111-119.
- Soares, R. F., Allen, D. H., Kim, Y.-R., Berthelot, C., Soares, J. B., and Rentschler, M. E. (2008). "A computational model for predicting the effect of tire configuration on asphaltic pavement life." *Road Materials and Pavement Design*, 9(2), 271-289.
- Song, S. H., Paulino, G. H., and Buttlar, W. G. (2006). "A bilinear cohesive zone model tailored for fracture of asphalt concrete considering viscoelastic bulk material." *Engineering Fracture Mechanics*, 73(18), 2829-2848.
- Walubita, L. F., and Scullion, T. (2008). "Thin HMA Overlays in Texas: Mix Design and Laboratory Material Property Characterization." Report No. FHWA/TX-08/0-5598-1, Texas Transportation Institute, The Texas A&M University, College Station, Texas.

- Wilson, B., Scullion, T., and Estakhri, C. (2013). "Design and Construction Recommendations for Thin Overlays in Texas." FHWA/TX-13/0-6615-1, Texas Transportation Institute, The Texas A&M University, College Station, Texas.
- Wu, Z., Chen, X., Gaspard, K., and Zhang, Z. "Structural overlay design of flexible pavement by nondestructive test methods in Louisiana." *Proc., Proceedings of the TRB 87st annual meeting*, Transportation Research Board, 1-16.
- Yoo, P., Al-Qadi, I. L., Elseifi, M., and Janajreh, I. (2006). "Flexible pavement responses to different loading amplitudes considering layer interface condition and lateral shear forces." *The International Journal of Pavement Engineering*, 7(1), 73-86.
- You, T., Masad, E. A., Al-Rub, R. K. A., Kassem, E., and Little, D. N. (2014). "Calibration and Validation of a Comprehensive Constitutive Model for Asphalt Mixtures." *Transportation Research Record: Journal of the Transportation Research Board*, 2447(1), 13-22.
- Zhou, C., Huang, B., Shu, X., and Dong, Q. (2013). "Validating MEPDG with Tennessee pavement performance data." *Journal of Transportation Engineering*, 139(3), 306-312.

Appendix A

The models used to characterize the material properties and identification process are described here. In the following sections, as equation (A-1) indicates, it was hypothesized that the total strain is decomposed into a (recoverable) viscoelastic strain and an (irrecoverable) viscoplastic strain based on a small strain theory. For each strain, Schapery's nonlinear viscoelastic single-integral model (Schapery 1969) and Perzyna-type viscoplasticity (Perzyna 1971) with a generalized Drucker-Prager yield surface (Masad et al. 2007) were used in this study.

$$\boldsymbol{\varepsilon}_{ij} = \boldsymbol{\varepsilon}_{ij}^{ve} + \boldsymbol{\varepsilon}_{ij}^{vp} \quad (\text{A-1})$$

where $\boldsymbol{\varepsilon}_{ij}$, $\boldsymbol{\varepsilon}_{ij}^{ve}$, and $\boldsymbol{\varepsilon}_{ij}^{vp}$ are the total strain, viscoelastic strain, and viscoplastic strain, respectively.

It is noted that the bar indicates the values in an effective (undamaged) configuration in the following sections.

A.1 Viscoelastic Material Properties

Three-dimensional representation of Schapery's nonlinear viscoelastic single-integral constitutive model (Schapery 1969) can be expressed as (Lai and Bakker 1996):

$$\begin{aligned} \boldsymbol{\varepsilon}_{ij}^{ve}(t) = & \frac{1}{2} J_0 g_0 \bar{s}_{ij}(t) + \frac{1}{2} g_1 \int_0^t \Delta J^{(\psi' - \psi^\zeta)} \frac{d(g_2 \bar{s}_{ij}(\zeta))}{d\zeta} d\zeta \\ & + \frac{1}{9} B_0 g_0 \delta_{ij} \bar{\sigma}_{kk}(t) + \frac{1}{9} \delta_{ij} g_1 \int_0^t \Delta B^{(\psi' - \psi^\zeta)} \frac{d(g_2 \bar{\sigma}_{kk}(\zeta))}{d\zeta} d\zeta \end{aligned} \quad (\text{A-2})$$

where g_0 , g_1 , g_2 and a_σ are nonlinear viscoelastic parameters and equal to 1.0 in linear viscoelasticity. The variable g_0 is related to an instantaneous response, g_1 affects a transient response, and g_2 is the nonlinear parameter accounting for the loading rate effects on the creep response. The instantaneous shear and bulk compliance are represented by J_0 and B_0 ,

respectively. Transient shear compliance is represented by $\Delta J(t)$, and $\Delta B(t)$ is transient bulk compliance. The deviatoric stress tensor and the Kronecker delta are \bar{s}_{ij} and δ_{ij} , respectively.

For an applied uniaxial undamaged stress ($\bar{\sigma}_0$), equation (A-2) can be written as:

$$\varepsilon^{ve}(t) = g_0 D_0 \bar{\sigma}_0 + g_1 \int_0^t \Delta D^{(\psi^t - \psi^\zeta)} \frac{d(g_2 \bar{\sigma}_0)}{d\zeta} d\zeta \quad (\text{A-3})$$

D_0 and ΔD represent the uniaxial instantaneous and transient creep compliance at linear viscoelasticity, respectively. ψ^t is the reduced time and written by:

$$\psi^t = \int_0^t \frac{d\zeta}{a_T} \quad (\text{A-4})$$

where a_T is time-temperature shift factor. Based on frequency-temperature superposition concept, the time-temperature shift factors of each temperature for a reference temperature were obtained in Table 5.1 by constructing the dynamic modulus master curve from dynamic modulus test results at different frequencies and temperatures. ΔD is the transient compliance and can be expressed by:

$$\Delta D^{\psi^t} = \sum_{i=1}^I D_i \left[1 - \exp(-\lambda_i \psi^t) \right] \quad (\text{A-5})$$

where D_i and λ_i are the i^{th} Prony series coefficients, and I is the number of terms in Prony Series. Storage compliance (D') and loss compliance (D'') from the experimental data and Prony series equations are calculated as follows (Park and Schapery 1999):

$$\begin{aligned} (\text{Experiment}) \quad D' &= \|D^*\| \cos \theta; & D'' &= \|D^*\| \sin \theta \\ (\text{Prony Series}) \quad D' &= D_0 + \sum_{n=1}^N \frac{D_n}{1 + (\omega/\lambda_n)^2}; & D'' &= D_0 + \sum_{n=1}^N \left[\frac{1}{\lambda_n} \frac{D_n}{1 + (\omega/\lambda_n)^2} \right]^2 \end{aligned} \quad (\text{A-6})$$

where θ is phase angle, and ω is frequency. By minimizing the error between experimental data and Prony series equations, the coefficients D_n and λ_n are obtained and summarized in Table 5.1.

A.2 Viscoplastic Material Properties

The viscoplastic strain was extracted by subtracting the viscoelastic strain from the experimental total strain that was obtained from the static multiple stress creep-recovery test. The identified viscoelastic parameters as described above were used to calculate the viscoelastic strain. From equation (A-1), the rate of the total, $\dot{\epsilon}_{ij}$, is expressed as:

$$\dot{\epsilon}_{ij} = \dot{\epsilon}_{ij}^{ve} + \dot{\epsilon}_{ij}^{vp} \quad (\text{A-7})$$

where $\dot{\epsilon}_{ij}^{ve}$ and $\dot{\epsilon}_{ij}^{vp}$ are the rates of the viscoelastic strain and viscoplastic strain, respectively. The following viscoplastic flow rule was proposed by (Perzyna 1971):

$$\dot{\epsilon}_{ij}^{vp} = \Gamma^{vp} \left\langle \frac{f}{\sigma_y^0} \right\rangle^N \frac{\partial g}{\partial \bar{\sigma}_{ij}} \quad (\text{A-8})$$

where f is a yield function, σ_y^0 is a yield stress quantity, g is a viscoplastic potential function,

N is a viscoplastic rate sensitivity exponent, and $\langle \cdot \rangle$ is the Macaulay bracket defined by:

$$\langle x \rangle = \begin{cases} 0, & x < 0 \\ x, & x \geq 0 \end{cases} \quad (\text{A-9})$$

where Γ^{vp} is a viscoplastic viscosity parameter, so that $1/\Gamma^{vp}$ characterizes the viscoplastic relaxation time. In this study, the modified Drucker-Prager yield surface presented in Masad et al. (2007) is used and given by:

$$f = \bar{\tau}^{vp} - \alpha \bar{I}_1 - \kappa (p_{eff}) \leq 0 \quad (\text{A-10})$$

where α is a material parameter related to the material's internal friction, \bar{I}_1 is the first stress invariant, p_{eff} is an effective viscoplastic strain, $\bar{\tau}^{vp}$ is an undamaged deviatoric shear stress, and $\kappa(p_{eff})$ is an isotropic hardening function and expressed as (Lemaitre and Chaboche 1990):

$$\kappa(p_{eff}) = \kappa_0 + \kappa_1 \left\{ 1 - \exp \left[-\kappa_2 (p_{eff}) \right] \right\} \quad (\text{A-11})$$

where κ_0 , κ_1 , and κ_2 are material parameters, which define an initial yield stress, a saturated yield stress, and a strain hardening rate, respectively. Moreover, the viscoplastic potential function, g , can be written by:

$$g = \bar{\tau}^{vp} - \beta \bar{I}_1 \quad (\text{A-12})$$

where β represents the dilation or contraction behavior of the material. It is noted that in this study a non-associated flow rule (i.e., $g \neq f$) is used since the use of an associated flow (i.e., $g = f$) overestimates the dilation viscoplastic strain compared to experimental measurements for pressure-dependent materials (Masad et al. 2007; Masad et al. 2005). The effective viscoplastic strain, p_{eff} in equations (A-10) and (A-11) can be expressed as:

$$p_{eff} = A^{-1} \sqrt{\varepsilon_{ij}^{vp} \varepsilon_{ij}^{vp}} \quad (\text{A-13})$$

where

$$A = \sqrt{1 + 2 \left(\frac{0.5 + \beta/3}{1 - \beta/3} \right)^2} \quad (\text{A-14})$$

The viscoplastic dynamic yield surface is written as:

$$\chi^{vp} = \bar{\tau}^{vp} - \alpha \bar{I}_1 - \kappa_0 - \kappa_1 \left[1 - \exp(-\kappa_2 p_{eff}) \right] - \sigma_y^0 \left(\frac{\dot{\gamma}^{vp}}{\Gamma^{vp}} \right)^{1/N} \cong 0 \quad (\text{A-15})$$

where $\dot{\gamma}^{vp}$ is a viscoplastic strain rate. Note that σ_y^0 was assumed to be 100 KPa because σ_y^0 was varied proportionally by the change of Γ^{vp} . Rearranging equation (A-15) gives:

$$\frac{\Delta\gamma^{vp}}{\Delta t} = \Gamma^{vp} \left\{ \frac{\bar{\tau}^{vp} - \alpha\bar{I}_1 - \kappa_0 - \kappa_1 [1 - \exp(-\kappa_2 p_{eff})]}{\sigma_y^0} \right\}^N \quad (A-16)$$

where $\Delta\gamma^{vp}$ can be calculated by:

$$\Delta\gamma^{vp} = \frac{\Delta\varepsilon_1^{vp,t}}{\partial g / \partial \sigma_1} = \frac{\Delta\varepsilon_1^{vp,t}}{\left(1 - \beta/3\right)} \quad (A-17)$$

where σ_1 and ε_1 are principal stress and strain, respectively. β presents the dilation or contraction behavior of the material. In this study, α and β were assumed to be 0.25 and 0.20, respectively, which were based on previous investigations by others (Masad et al. 2007; Seibi et al. 2001).

By selecting a specific level of $\Delta\gamma^{vp}/\Delta t$, times for each stress were found, then the viscoplastic strain at the corresponding times were determined. Rearranging equation (A-15) provides:

$$\bar{\tau}^{vp} - \alpha\bar{I}_1 = C - \kappa_1 \exp(-\kappa_2 p_{eff}) \quad (A-18)$$

where

$$C = \sigma_y^0 \left(\frac{\Delta\gamma^{vp}}{\Delta t \Gamma^{vp}} \right)^{1/N} + \kappa_0 + \kappa_1 \quad (A-19)$$

By minimizing the error between the experimental data and the prediction using equation (A-18), κ_1 and κ_2 were obtained. Then, the remaining viscoplastic parameters such as Γ^{vp} and N were determined by minimizing the error between the experimental results of $\Delta\gamma^{vp}/\Delta t$ for different stress levels and the prediction using equation (A-16). For more detail on the identification

procedure of the viscoplastic properties used in this study, refer to You et al. (2014). The viscoplastic model parameters are summarized in Table 5.2.

A.3 Fracture Properties

The fracture process zone (FPZ) is a nonlinear zone characterized by progressive softening, for which the stress decreases at increasing deformation. The nonlinear softening zone is surrounded by a non-softening nonlinear zone, which represents material inelasticity. Bazant and Planas (1997) skillfully classified the fracture process behavior in certain materials into three types: brittle, ductile, and quasi-brittle. Each type represents different relative sizes of those two nonlinear zones (i.e., softening and non-softening nonlinear zones). Figure A.1 presents the third type of behavior, the so-called quasi-brittle fracture. It includes situations in which a major part of the nonlinear zone undergoes progressive damage with material softening due to microcracking, void formation, interface breakages, frictional slips, and others. The softening zone is then surrounded by the inelastic material yielding zone, which is much smaller than the softening zone. This behavior includes a relatively large FPZ, as shown in the figure. Asphaltic paving mixtures are usually classified as quasi-brittle materials (Bazant and Planas 1997; Duan et al. 2006; Kim et al. 2008).

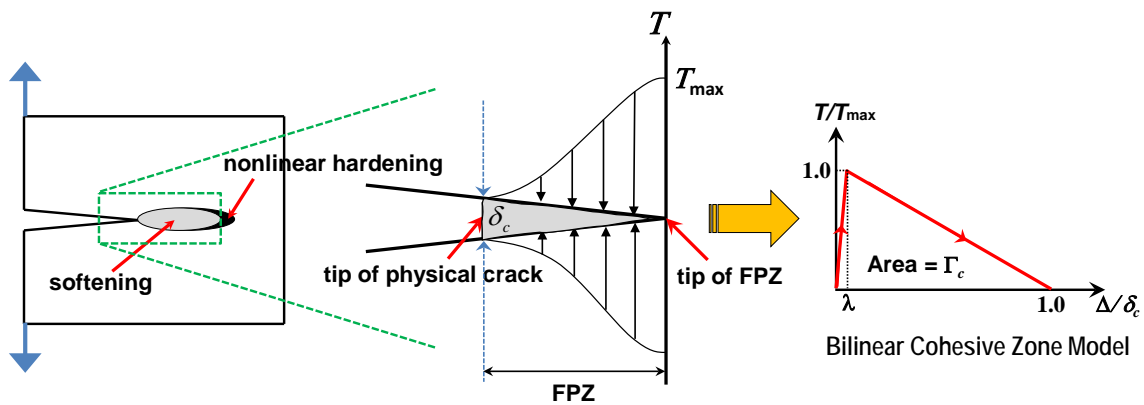


Figure A.1 Schematic illustration of FPZ of typical quasi-brittle materials

Cohesive zone models regard fracture as a gradual phenomenon in which separation (Δ) takes place across an extended crack tip (or cohesive zone) and where fracture is resisted by cohesive tractions (T). The cohesive zone effectively describes the material resistance when material elements are being displaced. Equations relating normal and tangential displacement jumps across the cohesive surfaces with the proper tractions define a cohesive zone model. Among numerous cohesive zone models developed for different specific purposes, this study used an intrinsic bilinear cohesive zone model (Espinosa and Zavattieri 2003; Geubelle and Baylor 1998; Song et al. 2006). As shown in Figure A.1, the model assumes that there is a recoverable linear elastic behavior until the traction (T) reaches a peak value, or cohesive strength (T_{\max}) at a corresponding separation in the traction-separation curve. At that point, a non-dimensional displacement (λ) can be identified and used to adjust the initial slope in the recoverable linear elastic part of the cohesive law. This capability of the bilinear model to adjust the initial slope is significant because it can alleviate the artificial compliance inherent to intrinsic cohesive zone models. The λ value has been determined through a convergence study designed to find a sufficiently small value to guarantee a level of initial stiffness that renders insignificant artificial compliance of the cohesive zone model. It was observed that a numerical convergence can be met when the effective displacement is smaller than 0.0005, which has been used for simulations in this study. Upon damage initiation, T varies from T_{\max} to 0 when a critical displacement (δ_c) is reached and the faces of the cohesive element are fully and irreversibly separated. The cohesive zone fracture energy (Γ_c), which is the locally estimated fracture toughness, can then be calculated by computing the area below the bilinear traction-separation curve with peak traction (T_{\max}) and critical displacement (δ_c) as follows:

$$\Gamma_c = \frac{1}{2} \delta_c T_{\max} \quad (\text{A-20})$$

Fracture properties were determined by integrating experimental tests with computational simulations of the SCB fracture tests. This was implemented to identify fracture characteristics along the fracture process zone (FPZ) where cracks initiate and propagate through the SCB specimens. Cohesive zone fracture was incorporated into finite element simulation to represent the fracture behavior of the materials.

Figure A.2 presents a three-dimensional finite element model, where six-node linear triangular prism elements (C3D6) were used for a bulk specimen. Eight-node, zero-thickness three-dimensional cohesive elements (COH3D8) were embedded along the center of the model to permit mode I cracking growth in the simulation of SCB testing. The bilinear cohesive zone model illustrated in Figure A.1 was used to simulate fracture in the middle of the SCB specimen as the opening displacements increased. It should be noted that there were several limitations involved in the simulations as a result of only considering homogenous and isotropic material and opening mode crack, which may not represent the true fracture process of specimens specially tested at the ambient temperatures where heterogeneity (i.e., microstructural characteristics) and other fracture modes (i.e., mixed-mode cracks) cannot be negligible.

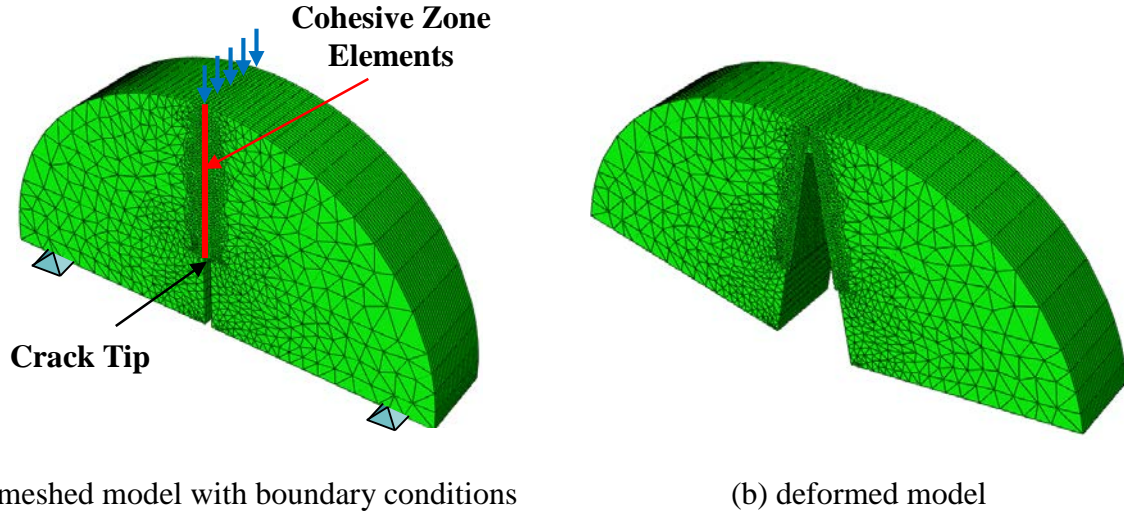


Figure A.2 A finite element modeling of the SCB testing

Among the cohesive zone fracture properties in the bilinear model, T_{\max} and I_c for each case were determined through the calibration process until a good match between test results and numerical simulations was observed. The identified fracture properties for different loading rates are summarized in Table 5.3.

A.4 Viscodamage Material Properties

In continuum damage mechanics, the damage density, ϕ , has a range from 0 to 1, where $\phi = 0$ means that the material is intact, while $\phi = 1$ means that the material is fully damaged, expressed as:

$$\phi(t) = 1 - \frac{\sigma(t)}{\bar{\sigma}(t)} \quad (\text{A-21})$$

where $\sigma(t)$ is the nominal (damaged) stress that was measured from a cohesive element located in a crack-tip (see Figure A.2) during the SCB test simulation with the fracture properties obtained above. The effective (undamaged) stress, $\bar{\sigma}$, was calculated from an element in the

same location during the SCB test without considering fracture of the material. The thermo-viscodamage evolution law is written as (Darabi et al. 2013):

$$\dot{\phi} = \frac{\Gamma_0^{vd}}{a_T} \left[\frac{\bar{Y}}{Y_0} \right]^q (1-\phi)^2 (\varepsilon_{eff}^{Tot})^k = \frac{\Gamma_0^{vd}}{a_T} \left[\frac{\bar{\tau}^{vd} - \alpha \bar{I}_1}{Y_0} \right]^q (1-\phi)^2 (\varepsilon_{eff}^{Tot})^k \quad (\text{A-22})$$

where Γ_0^{vd} is the viscodamage viscosity, \bar{Y} is the damage driving force in the effective configuration, Y_0 is the reference damage force, q is the stress dependency parameter, k is the strain dependency parameter, and ε_{eff}^{Tot} , total effective strain, is written as $\sqrt{\varepsilon_{ij} \varepsilon_{ij}}$. Note that the total strain (ε_{ij}) is composed of the viscoelastic strain (ε_{ij}^{ve}) and viscoplastic strain (ε_{ij}^{vp}). Taking the natural logarithm of both sides of equation (A-22) yields:

$$\text{Ln}(\dot{\phi}) = \text{Ln}\left(\frac{\Gamma_0^{vd}}{a_T}\right) + q \text{Ln}\left[\frac{\bar{\tau}^{vd} - \alpha \bar{I}_1}{Y_0}\right] + k \text{Ln}(\varepsilon_{eff}^{Tot}) + A \quad (\text{A-23})$$

where A is constant. The first, third, and fourth terms ($\frac{\Gamma_0^{vd}}{a_T}$, $k \text{Ln}(\varepsilon_{eff}^{Tot})$, A) in the right-hand side of equation (A-23) at a fixed effective strain level (ε_{eff}^{Tot}) are constant. To obtain q , the diagram of the damage density rate and \bar{Y}/Y_0 at different strain levels is plotted. As shown in Figure A.3

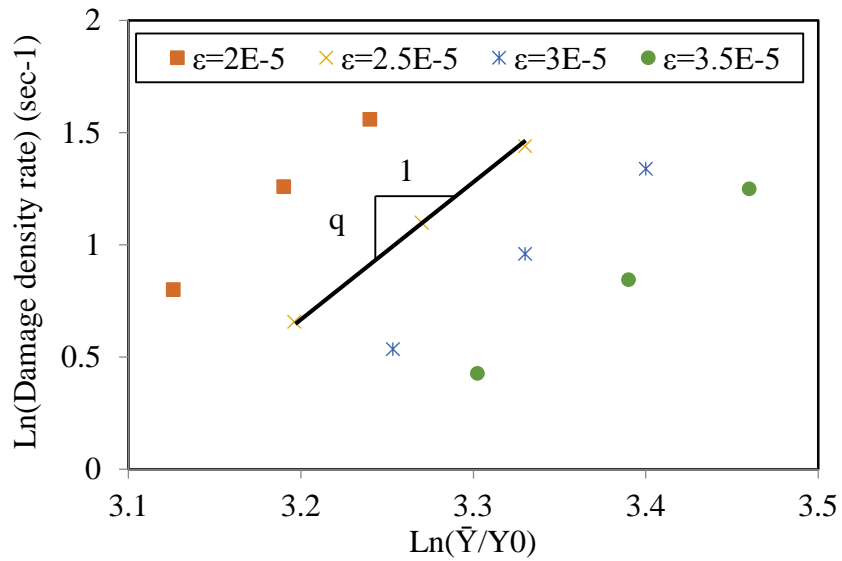
(a), q can be obtained as the slope of the lines. Similarly, the first, second, and fourth terms ($\frac{\Gamma_0^{vd}}{a_T}$,

$q \text{Ln}\left[\frac{\bar{\tau}^{vd} - \alpha \bar{I}_1}{Y_0}\right]$, A) in the right-hand side of equation (A-23) at a fixed \bar{Y}/Y_0 are constant. The

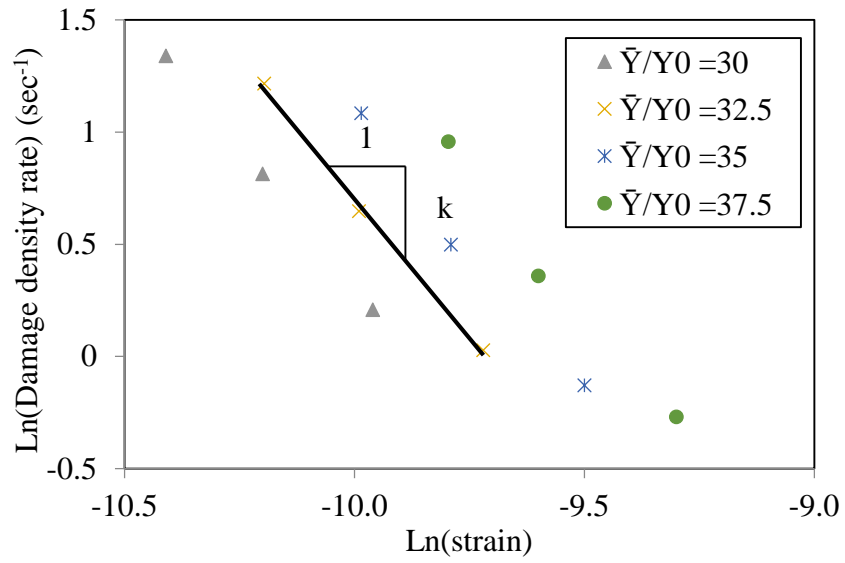
diagram of the rate of damage density and the effective strain at different \bar{Y}/Y_0 values is plotted in Figure A.3 (b), where k can be obtained as the slope of the lines. The intersections between the

lines and Y-axis are used to obtain $\frac{\Gamma_0^{vd}}{a_T}$, where the intersections in Figure A.3 (a) are the sum of

the first and third terms in the right-hand side of equation (A-23) and the intersections in Figure A.3 (b) are the sum of the first two terms in the right-hand side of equation (A-23). The rate of the damage density are zero on the Y-axis, while the damage density is calculated different strain levels in Figure A.3 (a) and at different \bar{Y}/Y_0 in Figure A.3 (b). The obtained viscodamage parameters are summarized in Table 5.4. For more detail on the identification procedure of the viscodamage properties used in this study, see You et al. (2014).



(a)



(b)

Figure A.3 (a) Diagram of damage density rate and \bar{Y}/Y_0 at different strain levels and (b) diagram of damage density rate and the effective strain at different \bar{Y}/Y_0 values